Title
Principles of Quantum Dot Photoexcited Charge Transfer

Author
Ding, Tina Xin

Publication Date
2016

Peer reviewed|Thesis/dissertation

Principles of Quantum Dot Photoexcited Charge Transfer

by

Tina Xin Ding

A dissertation submitted in partial satisfaction of the requirements for the degree of

Doctor of Philosophy

in

Chemistry

in the

Graduate Division

of the

University of California, Berkeley

Committee in charge:

Professor A. Paul Alivisatos, Chair
Professor Stephen R. Leone
Professor Ahmet Yildiz

Fall 2016

Abstract

Principles of Quantum Dot Photoexcited Charge Transfer

by

Tina Xin Ding

Doctors of Philosophy in Chemistry

University of California, Berkeley

Professor A. Paul Alivisatos, Chair

Photoexcited charge transfer is essential to light energy conversion processes in photosynthesis and solar cells. While fundamental theories governing these molecular and bulk charge transfer reactions are well established, the same level of understanding and agreement for nanoscale systems has not been achieved. It is essential to address this knowledge gap, as nanomaterials are becoming attractive candidates for optoelectronics and electrocatalysis. In this dissertation, hole transfer from high photoluminescence quantum yield CdSe-core CdS-shell semiconductor nanocrystal quantum dots to covalently linked molecular ferrocene acceptors is investigated in the context of Marcus Theory of Electron Transfer (Nobel Prize Chemistry 1992). This model quantum dot donor-acceptor system was thoughtfully designed to address the unique properties of QDs that complicate the proper characterization of the rate constants.

In this model system, modulating the electronic coupling and thermodynamic driving force for the reaction was done reliably and the hole transfer rate constant per acceptor, k_{ht}, was extracted by measuring steady-state and transient photoluminescence to determine the photoluminescence quantum yield in conjunction with quantitative NMR to determine the number of bound acceptors. Our studies varied the electronic coupling by four orders of magnitude by changing the shell thickness and the alkyl chain length. We find that there is a family of universal curves for PLQY as a function of coverage, spanning linear to nonlinear which depends critically on the ratio of the total hole transfer rate to the sum of the native recombination rates in the QD. Thermodynamic driving force was explored by molecular functionalizations on ferrocene that change the oxidation potentials of the acceptor. The rate's dependence on the driving force elucidated that there is no Marcus inverted region, and a new multistate model was posited to explain the result.

Parameters that affect the reorganization energy such as the surface ligands were also explored. Our model charge transfer system allowed us to examine the rate of thiol ligand exchange with surface oleates to determine the rate law and the rate order, and explore mechanisms of this exchange reaction. Single particle absorption and photoluminescence via fluorescence and photothermal microscopy were applied to examine photophysical properties of single QDs. We examined how fluorescence and absorption degrade over time and the heterogeneity of photoluminescence quantum yield in a given sample.

Acknowledgement

I am grateful for the opportunity to conduct my doctorate studies at UC Berkeley. My time here has been enriching and fulfilling both intellectually and personally.

I would like to thank my advisor Paul Alivisatos, for providing me with encouragement and support throughout my PhD years. I would like to thank him for pushing me to cultivate my own scientific questions and guiding me to answer them through the research cycle. I thank him for his warm personality and I especially appreciate his insightful perspectives on scientific topics and how to grow as an independent researcher.

I would like to thank my lab mate and very good friend Jacob Olshansky for the day-to-day conversations about charge transfer, quantum dots, and random discussions on life.

I would like to thank the other members of the Charge Transfer subgroup, especially Nima Balan and Erin O'Brien, for the uplifting and insightful conversations about research. It was a delight to work together, discuss science together, and form a community where we cared for each other's work and benefited from each other in a virtuous cycle. My last three years in the Alivisatos group have been especially enjoyable because of this. It was through this that I understood the merits of a collaborative supportive research environment.

I would like to thank my parents, my best friends and fellow scientists Donatela Bellone and John Kochalka for the personal support throughout the last five years.

Contents

List of Figures

List of Tables

Chapter 1

Introduction

1.1 QD Charge Transfer Motivation

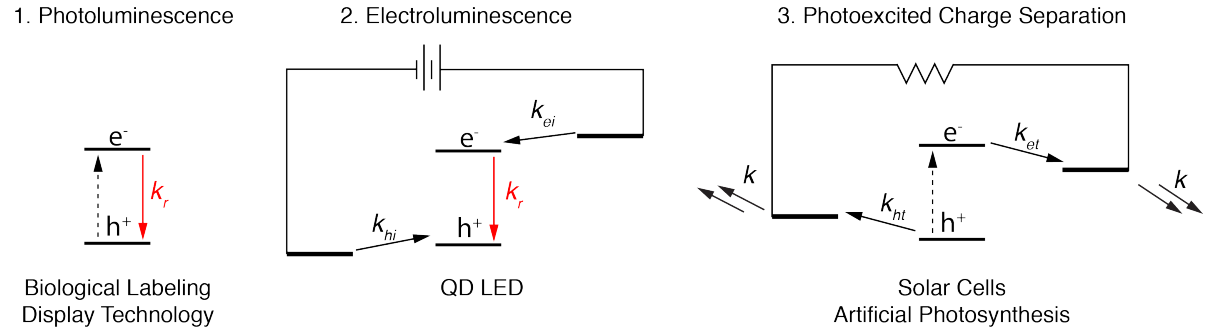

Figure 1.1: QD optical applications

Colloidal semiconductor nanocrystals, or quantum dots (QDs), have unique optical properties that make them attractive for a wide range of applications in displays [1], optoelectronics [2**?**], and biological labeling [3, 4]. These materials hold many advantages over traditional bulk semiconuctors and molecular dyes. QDs have tunable bandgaps due to quantum confinement, are more easily processed than bulk semiconductors because they are made in solution, and exhibit better photostability than molecular dyes because the exciton is more spatially delocalized.

Upon photoexcitation, the exciton in the QD can either recombine to emit a photon of light (usually visible), dissociate via charge transfer to native or engineered acceptors. Controlling the rate constants that govern these two competing pathways will tailor the material for use either in fluorescence applications like displays and biological labeling, or in solar energy conversion applications like QD sensitized solar cells [5] and QD photocatalysis. Therefore, the successful implementation of these materials for these two applications relies on an understanding of system parameters that govern the rate constants of these pathways.

Figure 1.1 shows the three main categories of QD applications. The first application, which relies on the photoluminescent properties of QDs is the most mature, with technologies in biological labeling (Invitrogen) and displays (Nanosys) being commercially available. Industry and academia are currently actively pursuing the second type of application, electroluminescence. The aim is to replace the emitter material in organic light emitting diodes

(LED) with QDs which have greater photostability. The last application, to drive the photoexcited charges to do useful work like create electricity or drive other useful chemical reactions, has great potential as a means of cheap clean energy. In all these applications, rate constants govern the reaction pathways. An understanding of the parameters that govern these rate constants would help us elucidate ways to design systems where desirable pathways are enhanced and undesirable pathways are mitigated.

1.2 Classic Marcus Theory for Charge Transfer

The Marcus Theory for Charge Transfer, developed in the 1960s by Rudy Marcus who won the 1980 Nobel Prize in Chemistry for this seminal work, relates the charge transfer rate constant, k_{ct}, between a donor and acceptor to thermodynamic driving force -ΔG, electronic coupling between the donor and acceptor H_{ab}, and reorganization energy λ (equation 1.1) [6].

$$k_{ct} = \frac{2\pi}{\hbar}|H_{ab}|^2 \frac{1}{\sqrt{4\pi\lambda k_b T}} \exp\Big(-\frac{(\lambda + \Delta G)^2}{4\lambda k_b T}\Big) \tag{1.1}$$

The relationship has a similar functional form to transition-state theory, which describes chemical reactions that result in structural change. The reorganization energy λ is the energy of the nuclear rearrangement to achieve the configuration of the final state without transferring the charge. Electron transfer reactions often occur in polar solvents, where the dipole of the solvent must change as the charge moves in the reaction. This solvent reorganization term can be significant and thus affects the rate constant substantially.

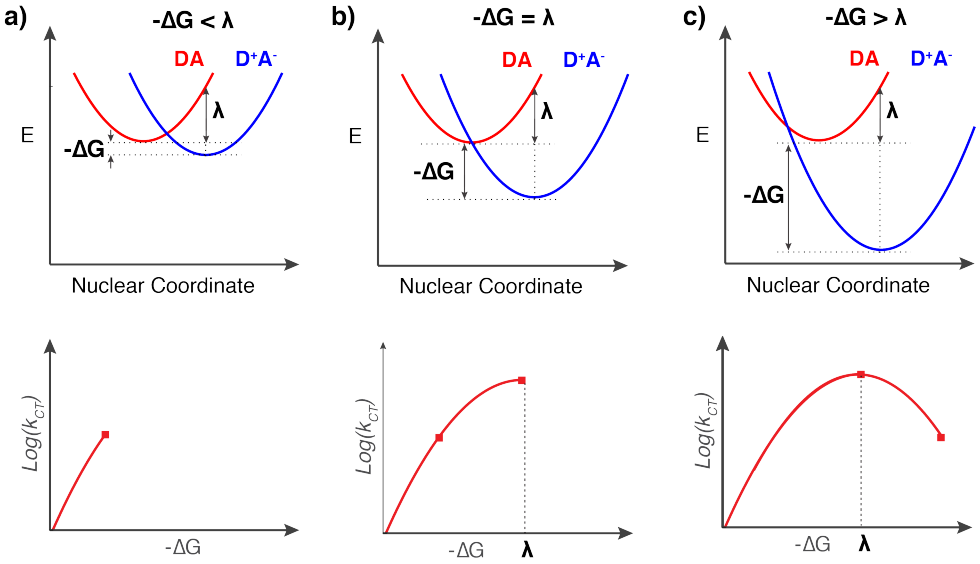

Figure 1.2: Marcus Parabolas of three different -ΔG

The charge transfer reaction can be best represented by overlapping Marcus parabolas, which represent the initial (red parabola) and final (blue parabola) states of the reaction as harmonic oscillators, with energy as the y axis and nuclear position as the x axis [Figure 1.2]

. Three different cases with varying -ΔG are depicted in Figure 1.2, to illustrate how the rate increases then decreases with increasing driving force. The intersection of the two parabolas represent the nuclear configuration in which the two states are inseparable, where a transition state would be in a typical chemical reaction. Thermal fluctuations in the environment lead the reactant to reach this energy state, from which it can transfer the charge. λ is also denoted in the figure, showing where the energy difference between the minimum of initial state and the energy where the reactant surface has the same nuclear coordinates as the minimum of the product state.

Like any chemical reaction, the rate constant depends on the Gibbs free energy of activation, $\Delta G^{\ddagger}$, which is the energy difference between the minimum of the initial state (red parabola) and the intersection of the two parabolas. $\Delta G^{\ddagger}$ can be rewritten in terms of ΔG and λ to produce equation 1.1.

Figure 1.2 demonstrates the three instances of -ΔG that lead to the reaction rate increasing to a maximum and eventually decreasing once more. As -ΔG first increases from panel a to panel b, the activation energy barrier is reduced to zero. In panel b, -ΔG is the same as λ, and $\Delta G^{\ddagger} = 0$. The reaction rate is therefore at a maximum since no thermal activation is necessary. As the -ΔG becomes even larger and the blue parabola moves further down, the activation energy barrier is recovered and the rate thereby decreases. In fact, the reaction has become so exergonic that the nuclear coordinates must move in the opposite nuclear direction from the path of the reaction in order for the electron to transfer.

These parabolas explain the rate's depencence on driving force, but as shown in equation 1.1, it also depends on other parameters like H_{ab} and λ. H_{ab} represents the wavefunction overlap between the donor and acceptor states, which depends on the material between them and how insulating it is to transporting charge. The rate's dependence on distance and the material between the donor and acceptor is represented empirically by equation 1.2, where β is the damping coefficient, which is related to the height of the energy barrier of the material and d is the distance of this material. This super-exchange charge transfer relationship holds true for the nonadiabatic charge transfer, when the coupling is weak so that the initial and final states are separate parabolas as is the case for the systems explored in this text.

$$k = k_o \exp(-\beta d) \tag{1.2}$$

The reorganization energy λ varies depending on the dielectric of the environment. Nonpolar solvents have λ of around 0.1 eV while solvents like water have λ around 1 eV. To achieve fast charge transfer without wasting energy, a system should ideally have low reorganization energy and a driving force that is equal to the reorganization energy (Figure 1.2b) with strong coupling.

Marcus Theory was conceptually developed in the 1960s [6], and was experimentally proven in 1980 [7]. The theory, especially its unexpected inverted region (Figure 1.2c) and the importance of the reorganization energy, helped explain many applications such as the rate constants of the cascade of charge transfer reactions in natural photosynthesis [6].

1.3 Marcus Theory Applied to QDs

While the development of Marcus electron transfer theory has clarified the field of molecular charge transfer, the same level of understanding and agreement has not yet been achieved for its nanocrystal analogue. Figure 1.3a shows the first experimental demonstration of the Marcus inverted region in molecular systems, a plot of the rate's dependence on driving force for an intramolecular electron transfer system [7]. As QDs are being considered for solar-energy conversion applications, there is a growing body of spectroscopic work examining charge transfer rates from QDs to molecular charge acceptors typically physisorbed onto their surface. A review on QD charge transfer compiled rate constants and driving forces obtained from literature, and finds that the rate's relationship to driving force lacks a discernable trend [8], as shown in Figure 1.3b. We seek to investigate the origins of this inconsistency in literature, identify the challenges unique to QD systems, and design a model QD donor-molecular acceptor system from which we can obtain the most reliable information regarding the rate's dependence on electronic coupling, driving force, and reorganization energy. By using a well-defined donor-acceptor system, we can reliably explore charge transfer in the context of Marcus Theory to shed insight on QD systems.

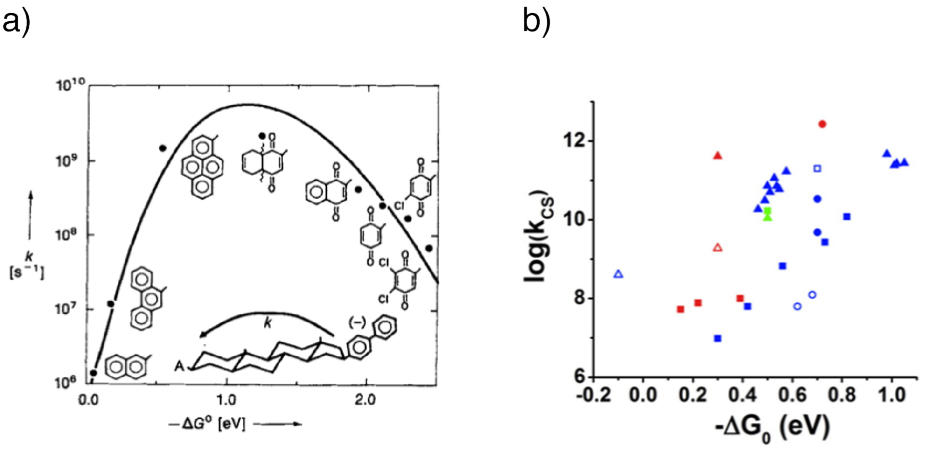

Figure 1.3: Molecular versus QD charge transfer's dependence on driving force. Reprinted (adapted) with permission from [8][9]. Copyright (2016) American Chemical Society.

The work highlighted in this dissertation specifically focuses on understanding hole transfer (HT) from photoexcited QDs to molecular acceptors that are functionalized on the surface. In the literature, electron transfer studies greatly outnumber hole transfer studies, despite hole transfer being the limiting factor to the efficiency of QD solar applications. The successful implementation of these applications relies on the rate of hole transfer to the intended acceptor outcompeting the rate of irreversible oxidation and degradation of the semiconductor, which is often enhanced through surface traps in the quantum dot. The intrinsic rate of hole transfer is typically very slow compared to electron transfer, making it even more vulnerable to these competing non-radiative trapping processes. In QD sensitized solar cells, the filling of the photoinduced hole by redox mediators lags behind the picosecond electron injection into TiO_2 [9]. In colloidal photocatalytic hydrogen evolution, sacrificial hole acceptors are often employed to outcompete oxidation of the semiconductor

material by the photogenerated hole [5]. By investigating the parameters that influence the rate constants of hole transfer, we can design better photocatalytic systems in which the hole transfer rate constant can be enhanced to be competitive with electron transfer rates.

Chapter 2 will present the design, synthesis, and characterization of a model hole transfer system that will be extensively studied throughout this dissertation. The chapter will highlight the reasons why the system was chosen and the methodologies that will be implemented to determine the hole transfer rate constants. Chapter 3 will utilize the methods of characterization described in Chapter 2 to study hole transfer rate constants as a function of electronic coupling and thermodynamic driving force in the context of Marcus Theory. Both its agreement and deviation from classic theory will be discussed in detail. Chapter 4 will explore the surface ligands on QDs that affect the reorganization energy of the charge transfer system. It will present various tools for understanding the surface structure as well as utilize the model charge transfer system presented in Chapter 2 to study the kinetics of the ligand exchange on the QD surface. Lastly, Chapter 5 will delve into the use of optical microscopy to study the photophysics of quantum dots on a single particle level. Here, we seek to understand basic photophysical properties of single quantum dots, such as the photoluminescent quantum yield. By developing a highly sensitive photothermal microscopy technique, we explore the simultaneous measurement of heat and photoluminescence of single QDs.

Chapter 2

Design, Synthesis, and Characterization of a Model System

We attribute the inconsistencies in the QD charge transfer literature discussed in Chapter 1 to four main challenges unique to QDs that make this system more difficult to characterize than for the pure molecular case, as shown in Figure 2.1. In order to develop a thorough understanding of the dependence of driving force, electronic coupling, and reorganization energy on charge transfer rate constants, it is pivotal that we understand these challenges and design a model system that addresses and overcomes these limitations. Some of these challenges were discussed in Knowles et al [8].

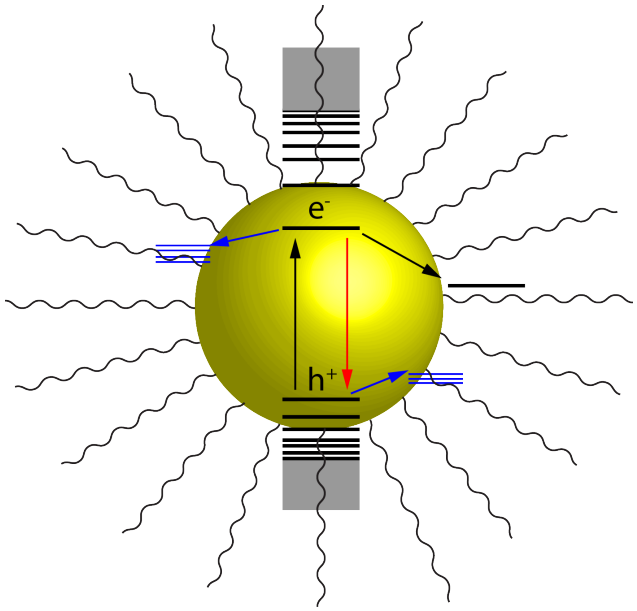

Figure 2.1: Cartoon of a QD and its de-excitation pathways

1. Competing trap states of unknown spatial and energetic position

    - Unlike molecules, QDs exhibit trap states of ill-defined energetic and spatial distribution[10][11]. Some of these states come from lattice defects and most of them come from dangling bonds on the surface of these particles. Due to the

presence of various facets on the surface and the heterogeneity of QD samples, it is difficult to determine the number of traps, where they are located on the quantum dot, and where they lie energetically. Charge transfer to these trap states results in coupling with phonons that leads to nonradiative emission or radiative trap emission. Therefore, these exist as a distribution of nonradiative de-excitation pathways that diminishes the radiative bandedge quantum yield and convolutes with the lifetime decay. It is for this reason that native quantum dots such as CdSe or CdS have PLQY typically lower than 10%. Furthermore, the distribution of these energy states fluctuate [11]. This results in lifetime decay data that are multiexponential, from which it is difficult to analyze and interpret the data.

2. Ill-defined coupling between donor and acceptor

    - The bulk of studies that exist in the literature report physisorption to be the interaction between the donor and acceptor. In these studies, molecular acceptors without binding groups are mixed in solution with the quantum dots. The "attached" molecules are not quantified and exist in a dynamic equilibrium with the concentration of free molecules in solution. Because of the weak energies associated with these interactions, the equilibrium of this physisorption is highly skewed to the left of the reaction, with the concentration in solution being orders of magnitude higher than the concentration "bound". Furthermore, there exists great heterogeneity in the physisorption, as the molecule can orient in many ways onto a surface. The existence of different surface facets further adds to this heterogeneity. The extent of these interactions make one system difficult to compare to another, as this physisorption interaction is likely to change from one acceptor to the next. In my experiments in the lab making QD-acceptor systems this way, I have found that the acceptors that are physisorbed to the surface often lose their optical properties. Electronic coupling via Van der Waals forces is much weaker than those achievable through covalent interactions [12, 13]. We therefore seek to bring clarity to the distance and rigidity of the interaction between the donor and acceptor in our work.

3. One to Thousands of Acceptors

    - QDs have surface areas on which one to thousands of acceptor ligands can bind. The rate measured will be for the total charge transfer rate of the system, Nk_{ht}, so normalization for the number of acceptor ligands on the surface, N, is pivotal for reliable comparison of k_{ht} across different donor-acceptor systems. We assume that each additional hole transfer pathway is additive and independent of the other pathways of the system, as given by equation 2.1. However, high coverage, we expect that there may be positive or negative cooperativity leading to deviations from this assumption. Inconsistencies in the method of measurement, especially regarding reporting single donor-single acceptor charge transfer rate constants (k_{ct}) versus single donor-multiple acceptor charge transfer rate constants (k_{NCT}), lead to drastically different values for similar systems[8]. Some groups have characterized the number of ligands bound indirectly using optical

methods [14, 15, 16]. In most of these previous studies, fitting based on a binding model that differentiates bound and free states is used to indirectly infer N. NMR, though difficult to measure due to the high concentration required for its measurement, allows one to directly differentiate between bound versus free ligands due to their different signatures in the NMR spectrum.

$$k_{NCT} = Nk_{CT} \tag{2.1}$$

4. Varying one parameter without the rest

   - This is the most easily overlooked point that will have a tremendous effect on the interpretation of the experimental data. For QD systems, this is especially important, as the driving force and the coupling are both affected by varying the size of the material. For example, smaller particles have higher driving force, but because the excitons are confined to a smaller region, there is greater overlap of the exciton wavefunction with the surface, resulting in greater electronic coupling between the donor and the acceptor. The QD literature is full of driving force studies that vary driving force by varying the size [**?**]. It is pivotal that we design an experiment where these parameters can be decoupled from each other.

2.1 Design of a Model Donor-Acceptor System

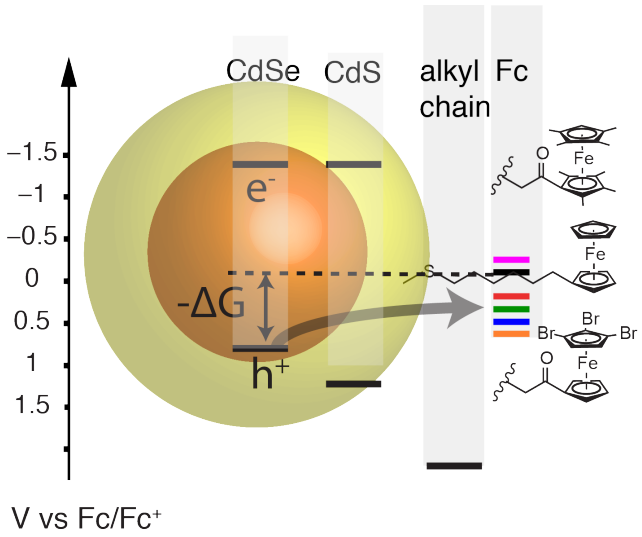

Figure 2.2: Cartoon depiction of the donor-acceptor system studied.

We designed a QD-donor molecular-acceptor system that addresses all the challenges noted in the last section, as shown in Figure 2.2. CdSe particles are shelled with a larger band gap material CdS which acts as an energetic barrier to the trapping pathways that lie on the surface. These heterostructures have high quantum yields and highly monoexponential lifetime decays that are readily interpretable [17]. Although the nonradiative pathways are now more suppressed, the shell also electronically insulates the QD, erecting a barrier to

the very charge transfer process for which it is designed. The careful balance of these two interplaying processes of mitigating undesirable traps while enhancing desirable traps is key to the photoenergy conversion applications of these QD systems.

For controllable tunability over the driving force of the charge transfer reaction, we chose ferrocene as the photoexcited hole acceptor. Ferrocene's oxidation potential, Fc/Fc^+, 0.64 V versus Standard Hydrogen Electrode, can be tuned by one Volt via changing the functional groups of its cyclopentadiene rings. This tunability allows us to control the driving force without changing any other parameter that affects the charge transfer rate constant. This will allow us to explore the rate's dependence on driving force and whether these systems behave like classic Marcus models.

The ferrocene molecules are linked to a saturated carbon chain with a thiol moeity that binds to cadmiums on the QD surface. This strong covalent bond ensures we have a well-defined distance between the donor and acceptor. We can tune the distance of the alkyl chain to change the strength of the coupling as well. The number of ferrocene acceptors will be measured by NMR and the hole transfer rate constant per acceptor k_{ht} will be determined.

2.2 Synthesis of QDs

CdSe-core CdS-shell QDs were synthesized in two main steps. For the rest of this chapter, we are going to look at properties through characterizations of these core-shell particles, specifically CdSe-core with 3 monolayer (ML), 5ML, and 7ML CdS shells.

2.2.1 CdSe-core

Cadmium oxide (CdO) (60 mg), octadecyxlphosphonic acid (ODPA) (280 mg), and trioctylphosphine oxide (TOPO) (3 g) were added to a 25ml flask and heated to 150 °C, at which point it was then switched to vacuum to pull off any low boiling impurities in the solvent for an hour. The reaction mixture was then heated to 350 °C, at which TOP (1.5 g) was slowly injected. A TOP-Se complex solution was prepared by sonicating trioctylphosphine (TOP) (1 mL) and Se (0.64 mg) until the black Se powder has coordinated to the phosphine, turning the solution clear. The reaction flask was heated to 370 °C at which point the TOP-Se mixture was swiftly injected with a 16 gauge needle. The reaction was stopped at 45 seconds and cooled. The purification procedure was done air-free as well. The solution was brought inside a glovebox, and methanol was added to the reaction to precipitate the nanocrystals. After centrifuging at 4000 rpm for 5 minutes, the supernantant was poured off, and the particles were resuspended in toluene. The steps of precipitation, centrifugation, and resuspension were repeated two more times to remove the free ligands in solution. The reaction conditions given here gave particles that were 3.8 nm in diameter, but changing the injection temperature and reaction temperature will produce different sizes. The CdSe particles are shown in Figure 2.3A of the TEM micrograph figure.

2.2.2 CdS shell

CdS shell growth was conducted by modifying a previously published procedure[17]. The amount of cadmium precursors in the synthesis was determined by calculating the

concentration of precursors required to grow the desired thickness of the shell using lattice parameters of the material. The cadmium precursor for CdS growth was made by mixing CdO with 10 equiv of oleic acid (OA) and the needed quantity of octadecene (ODE) to reach 0.2 M concentration of cadmium oleate, heating at 250 °C under argon until the solution turned clear, and degassing at 100 °C for 30 min. Appropriate amounts of octanethiol and ODE were mixed to prepare 0.2 M octanethiol solution, which served as the sulfur precursor. Depending on the desired thickness of CdS, the moles of precursors required were calculated, and the correct volume of the precursor solutions was subsequently injected together. A 50 mL three-neck round-bottom flask equipped with a reflux condenser and a thermocouple was charged with CdSe QDs (200 nmol measured by the first exciton[18]), 3 mL of oleylamine, and 3 mL of ODE. The mixture was heated to 310 °C to react, and the injections of the Cd and S precursors began at 250 °C at a rate of 3 mL/hour. Once the injections were finished, the flask was cooled, and the CdSe-core CdS-shell nanocrystals were isolated from the ligand mixture by precipitating the particles in acetone, redispersing them in hexane, and repeating this procedure two more times.

2.3 Physical Characterization of QDs

2.3.1 Transmission Electron Microscope (TEM)

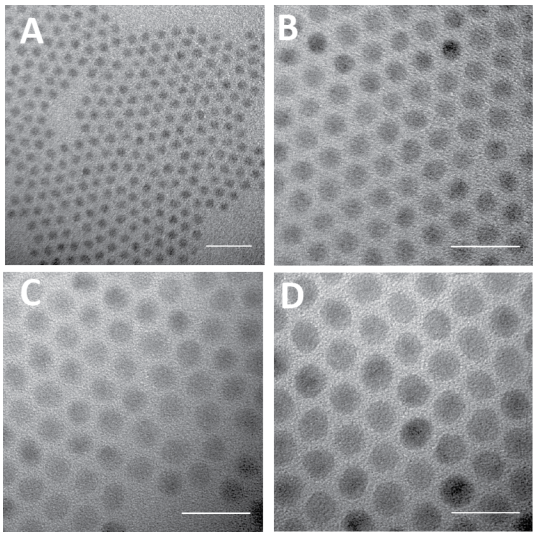

Figure 2.3: TEM images of A. CdSe (d = 3.8 nm) B. 3ML C. 5ML and D. 7ML CdSe/CdS QDs. Scale bars are all 20 nm.

The cleaned quantum dots in concentrations of tens of nM are drop-cast onto carbon film 400 square mesh copper grids (Electron Microscopy Sciences). Images were acquired on a FEI Tecnai T20 with a LaB_6 filament and 200 kV accelerating voltage. Figure 2.3 shows TEM images of the CdSe core (A), CdSe-core CdS-shell in B to D; The physical and optical properties of these sizes will be given throughout the section to demonstrate the effect of size on their relevant properties. These particles are used in further studies of electronic coupling as well, which is documented in Chapter 3.

2.3.2 X-ray Powder Diffraction (XRD)

XRD scans was collected on a Bruker GADDS Hi-Star D8 diffractometer with Co Kα ($\lambda = 1.790$ Å) operating at 45 kV/35 mA . Samples were prepared by drop casting concentrated nanocrystal solutions onto a silicon crystal plate. The pattern for CdSe and CdS show characteristic diffraction planes associated with the wurtzite crystal structure. Chalcogenide materials exist in the kinetically stable cubic zinc blende crystal structure and the thermodynamically stable and higher packing efficiency wurtzite structure. The wurtzite phase is accessible at high temperatures, which overcomes the high kinetic barrier. This is reflected in our synthesis, which is done at about 50 degrees higher temperature than zinc blende synthetic recipes.

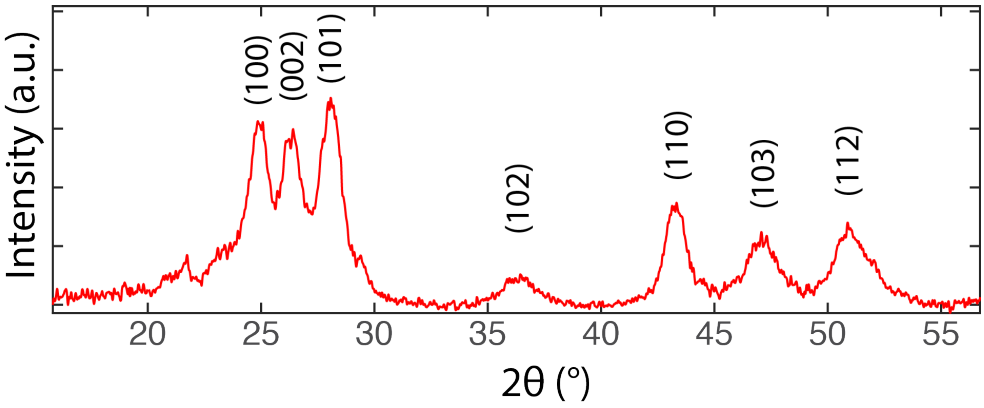

Figure 2.4: XRD spectra of CdSe-core CdS-shell

2.3.3 Quantitative NMR

The chemical nature and the coverage of the organic surface ligands on the QDs can be determined via proton and phosphorus NMR. Owing to the reactants in the synthesis of these materials, the ligands on the surface of the QDs are either OA or ODPA, both of which coordinate to excess surface cadmiums, as shown in Figure 2.5 . Cd-ODPA ligands are the Cd coordinating ligand in the CdSe system while Cd-OA are the Cd coordinating ligand in the CdS shell growth synthesis. ^{1}H NMR and ^{31}P NMR confirm the presence of both species.

Ligands bound to large species like nanoparticles and proteins have larger linewidth in the NMR spectra than their free molecule counterparts due to their slower tumbling rates. Free molecules have similarly long T_1 and T_2 relaxation times, as their fast molecular motion allows them to sample many frequencies with only a small fraction at the Lamor frequency. On the other hand, large species have long T_1 relaxation times and short T_2 relaxation times. The width of the NMR signal can be related to T_2 as expressed by equation 2.2 and leads to the signal broadening observed in ligands bound to QDs. This causes regions with distinct but closely spaced peaks to be unresolvable in NMRs of QDs, as is the case for the aliphatic region 0.5-2 ppm in proton NMR. However, the signature broadening is also a valuable tool for discerning whether the ligand is bound or free, which is very useful for our charge transfer studies in which the coupling between the donor and acceptor is well-defined.

$$W_{1/2} = \frac{1}{\pi T_2} \tag{2.2}$$

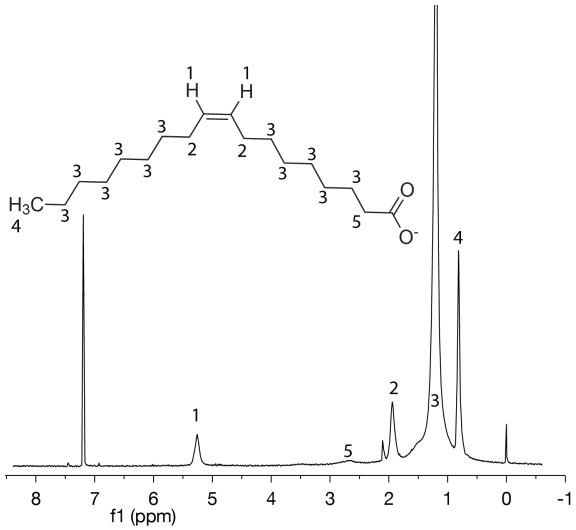

Figure 2.5: ^{1}NMR of bound oleic acid

Proton NMR shows the characteristic peak at 5.25 ppm associated with the vinyl bond in the center of the oleic acid chain (Figure2.5). ODPA has no signature outside the aliphatic region in proton NMR and would be difficult to differentiate from the aliphatic peaks of OA. The ratio of the vinyl peak to the aliphatic region does not match the ratio of the vinyl protons to aliphatic protons of oleic acid, indicating the presence of other ligands besides OA. Assuming that the rest of the aliphatic region of proton NMR that does not correspond to the integrated OA protons belongs to ODPA, we can determine the percentage of OA and ODPA on a given sample of QDs. Phosphorus NMR, discussed more in detail later, also confirms the presence of ODPA.

Quantitative NMR spectra of micromolar concentrations of CdSe/CdS core–shell particles were measured on a Bruker 400 MHz instrument. Digital ERETIC (Bruker Topspin) was used to determine the concentration of ligands, which is an instrumental implementation of the PULCON (pulse length based concentration determination) method[19]. In this method, a known concentration of a standard (10 mM of ferrocene in $CDCl_3$ in the current study) was measured on the instrument after tuning the probe and measuring the exact 90° radio frequency pulse. The ferrocene peak was integrated, and the known concentration was entered and stored into the software for that peak. When measuring the concentration of the ligand protons in the nanocrystal sample, the same receiver gain value was used, the probe was tuned, and the 90° pulse was determined and used. Digital ERETIC was implemented in the software by converting the absolute integration measured to concentration; at the same time, a synthetic peak was generated in the spectrum as a reference to concentration. Note that one can determine quantitative concentration without the software functionality as well, by comparing the absolute integration values divided by the number of scans of the known standard with that of the unknown concentration sample; this method is highlighted in reference [19]

2.3.4 Inductively Coupled Plasma (ICP)

Inductively Coupled Plasma (ICP) on the Cd ions of dissolved QDs are conducted to determine the concentration of Cd, from which using the sizes of the particles as determined by TEM and the lattice constants of the CdSe and CdS wurtzite material, we can determine the concentration of the QDs. To prepare a ICP sample, a measured volume of QDs are obtained from the stock, and the solvent is evaporated. Then, 0.5 ml of 12 M ICP-grade nitric acid was added to the dried QDs to dissolve the particles into free ions. After a few hours, a known quantity is obtained from this solution and diluted by a factor of 100 as the first concentration of a five concentration series for ICP measurements. The rest of the concentrations are two fold dilutions of the previous concentrations. This builds the same concentration series as the calibration curve obtained from Cd ICP standards. The samples are measured on an Optima 7000 DV ICP-AES (Perkins Elmer).

Knowing the concentration of QDs and concentration of ligands, we can determine the density of OA and ODPA ligands on the QD surface. More importantly, we can monitor the ligand environment over the course of the ligand exchange, and determine which and how much of the native ligands are displaced during the exchange to thiol ligands. Table 2.1 shows the ligand coverages for three sizes of QDs.

	QD diameter(nm)	OA_o	OA/nm^2	PA_o	PA/nm^2
3ML	6.4 ± 0.36	198	1.75	324	2.9
5ML	7.4 ± 0.54	413	2.34	368	2.1
7ML	8.9 ± 0.62	890	3.58	382	1.5

Table 2.1: Ligand Coverage on QDs

2.4 Optical Characterization of QDs

2.4.1 Steady-state Absorption

Absorbance spectra were acquired using a Shimadzu 3600 spectrophotometer with 1 nm increments with solvent background subtraction. Quantum dots of hundred nanomolar concentration in a quartz cuvette are represented by the colored spectra shown in Figure 2.6a. This is the same set of CdSe-CdS quantum dots with 3.8 nm diameter CdSe core and 3ML, 5ML, and 7ML CdS shell as shown in the TEM micrograph in Figure 2.3. Characteristic quantum dot spectra show the bandedge absorption and the discrete higher energy allowed discrete transitions overlayed with the density of states. The CdS shelling of the core leads to less quantum confinement causing a redshift of the absorption of the exciton bandedge. As there is greater volume of CdS in the particle, the absorption becomes dominated by the CdS absorption (bulk bandgap = 2.42 eV).

2.4.2 Steady-state Photoluminescence

Photoluminescence (PL) emission spectra were collected on a Horiba Jobin Yvon TRIAX 320 Fluorolog. Particles with the same sample preparation as for absorption are excited

at 505 nm. PL occurs at the bandedge and is Stoke-shifted by around 10-13 nm, shown in Figure 2.6. The emission linewidth of these particles are remarkably narrow, indicating there is high monodispersity.

2.4.3 Time-resolved Photoluminescence

Fluorescence lifetime was collected on a Picoquant Fluotime 300 with a PMA 175 detector and a pulsed LDH-P-C-405 diode laser (excitation wavelength of 407.1 nm). Decay measurements were taken at 1 MHz and 100 ps pulse width. From the time-resolved photoluminescence spectra of our set of three shelled QDs, we can fit the decay data to single exponentials and determine the total lifetime of the excited state, k_{tot}, in equation 2.3. The k_r for these three sizes are shown in Table 2.2. The decreasing values of k_r as a function of increasing particle size are expected as a result of the electron delocalization through the larger volumes, resulting in reduced wave function overlap with the hole that remains localized in the CdSe core[20].

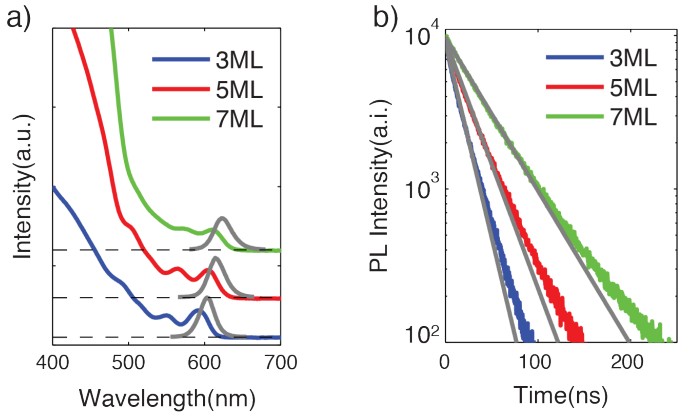

Figure 2.6: Steady-state and time-resolved optical spectra of QDs

$$PLQY = \frac{k_r}{k_r + k_{nr}} = \frac{k_r}{k_{tot}} \tag{2.3}$$

2.4.4 Quantum Yield Measurements

The photoluminescence quantum yield (PLQY) in equation 2.3 was determined via two methods, calibration to a reference dye, Rhodamine 6G, and measurement inside an integrating sphere. Both give the same results within error.

Method 1: Quantum yields were determined by measuring the fluorescence intensity of the nanocrystals at different concentrations (and therefore different absorption intensities) and comparing the slope against the known quantum yield of Rhodamine 6G. The absorption spectra were taken at four dilutions of the quantum dot sample and Rhodamine 6G sample. The fluorescence spectra of the two sets of samples were taken at the excitation wavelength that corresponds to the intersection of the QD and Rhodamine absorptions (the wavelength at which both samples are absorbing the same intensity of light). The integrated intensities

are plotted as a function of absorption intensity, from which the slopes were determined. Using the following equation, we determined the quantum yield of our QD sample.

$$PLQY = PLQY_{Rhd6G}(\frac{Grad_{QD}}{Grad_{Rhd6G}})(\frac{n^2_{QD}}{n^2_{Rhd6G}}) \tag{2.4}$$

where n is the refractive index and $Grad$ is the gradient of the PL-absorption relationship. The $PLQY$ of Rhodamine 6G is 0.95.

Method 2: Quantum yields were determined by using a home-built integrating sphere. A Fianium SC450 supercontinuum pulsed laser was used as a white light source, which provides 4 W average illumination from 470 nm to 2500 nm with more details described in Bronstein et al [21].

2.4.5 Summary of Optical Properties of the Three Core-Shell QD Sizes

PLQY and k_{tot} are used to determine the radiative rate constant k_r using equation 2.3. All optical properties of the three sizes of QDs (3ML, 5ML, and 7ML) and the CdSe core are summarized in Table 2.2.

	λ_{abs}(nm)	λ_{PL} (nm)	τ_r (ns^{-1})	k_r (ns^{-1})	$k_{nr}(ns^{-}1)$	PLQY
3ML	593	603	23	44	10	79%
5ML	604	614	32	31	5.3	86%
7ML	610	623	48	21	2.2	91%

Table 2.2: Optical Characterizations

2.5 Ferrocene Acceptor Ligand Synthesis and Characterization

The acceptors used in this study were either bought from Sigma Aldrich if they were commercially available or synthesized in lab. The addition of the thiol linker to the ferrocene acceptor was synthesized via the general steps shown in the schematic of Figure 2.7 and detailed as following, adapted from previous work[22, 23].

Friedel-Crafts acylation: Ferrocene (2.25 g, 12 mmol), 3-bromopropionyl chloride (1.7g, 10 mmol), and 20 ml of dichloromethane were loaded in a 50 ml 3-neck flask and placed in an ice bath. Under argon, $AlCl_3$ (1.3 g, 10 mmol) was added, followed by a solution color change from dark orange to dark purple. The ice bath was removed, and the flask was left to warm up to room temperature to react for 3 hours. To the reaction, 50 ml of 0.1 M HCl was added to quench unreacted $AlCl_3$. The product was extracted three times with dichloromethane, washed three times with water, and dried over $MgSO_4$. Column chromatography using hexane : ethyl acetate mixture (15:1) was conducted to purify the product which is an orange red slurry (I).

Keto Reduction: I (0.47g, 1.5mmol) was dissolved in 13 ml of tetrahydrofuran (THF) in an ice bath. Under argon, $NaBH_3CN$ (1.19 g, 19 mmol) was added. The ice bath was removed, and the solution was allowed to warm up to room temperature to react for 5 hours. The reaction was cooled to 0 °C, during which drops of 2 M NH_4OH were added until the reaction finished quenching. The product, was extracted with diethyl ether, washed

with brine three times, and dried with $MgSO_4$. Column chromatography using hexane was conducted to purify the product (II).

Thiolation: A solution of tetra-n-butylammonium fluoride in THF was added to a mixture of II and hexamethyldisilathiane cooled in an ice/NaCl bath. The mixture was allowed to warm to room temperature over 45 minutes. The reaction was then quenched by adding the solution to 10 ml of ice water. The organic layer was then diluted with diethyl ether and washed with water three times. The organic layer was collected and dried with $MgSO_4$ and the solvent was removed by rotary evaporation to yield an orange oil. Column chromatography with a hexane : ethyl acetate (10:1) solvent mixture separated the final product (III).

In the example shown in Figure 2.7, the molecular structure of the product was verified by proton NMR: ^{1}H NMR (400 MHz, $CDCl_3$): 4.10 (s, 5H), 4.05 (s, 4H), 2.55 (q, 2H), 2.45 (t, 2H), 1.81 (q, 2H), 1.35ppm (t, 1H) and shown in Figure 2.8. Ferrocene ligands in this paper are synthesized following this general set of procedures, with minor modifications, which will be mentioned when relevant in the text.

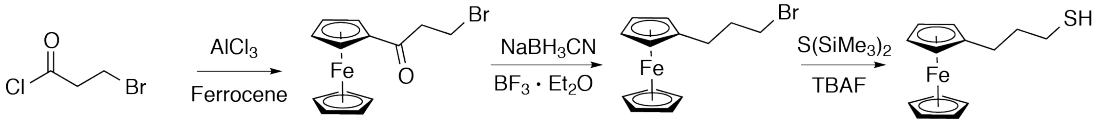

Figure 2.7: Thiol ligand functionalization of Ferrocene

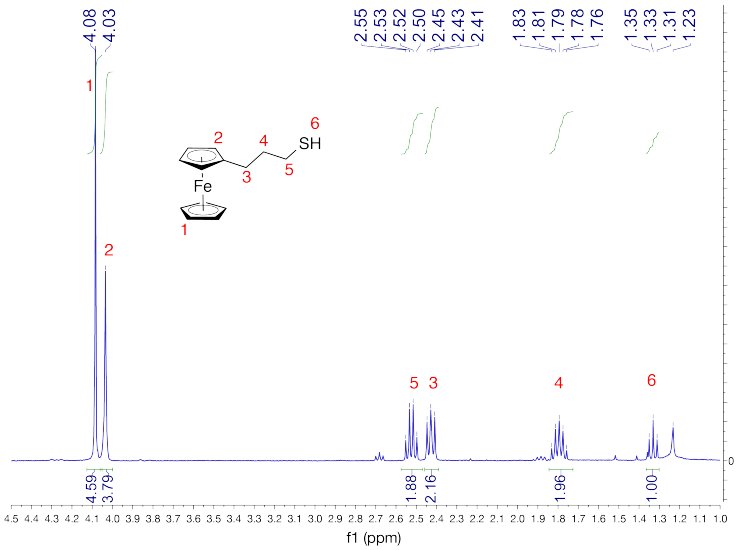

Figure 2.8: ^{1}NMR of the FcC3SH

2.6 QD-Fc System

2.6.1 Assembly and Characterization

The donor—acceptor system was prepared by controlled ligand exchange of the thiol-functionalized acceptor ligands with the native oleate ligand. Thiol ligands were mixed with

the QD samples, and surface oleates were exchanged with thiol ligands in tens of seconds, as the thiol has much a higher affinity for Cd than oleic acids[24]. The samples were then purified by precipitating the quantum dots with acetonitrile. The supernatants containing the free ligands were decanted and the particles were resuspended in a dispersible solvent like chloroform. The precipitation is then repeated two more times. We demonstrate that this cleaning method of using chloroform and acetonitrile do not affect the optical properties of the quantum dot. We have performed control experiments to verify that the PLQY remains the same within error over 12 iterations of these washing steps. This is due to the inert properties of aproptic solvents like acetonitrile as opposed to interacting protic solvents like methanol [25].

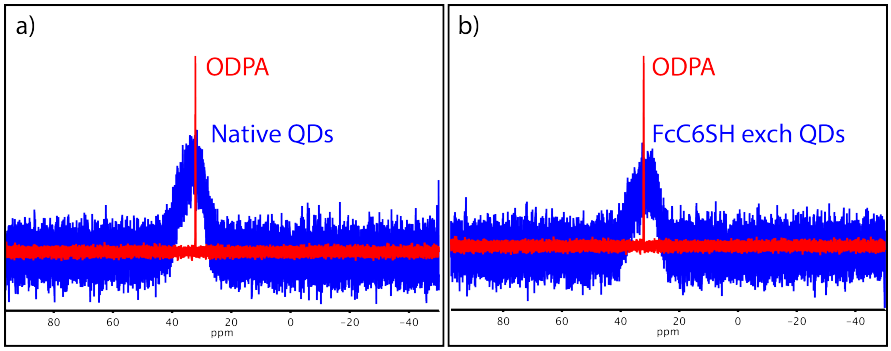

Figure 2.9: Phosphorus NMR

ODPA has also been shown to form very strong bonds on chalcogenide nanocrystal surfaces,[26, 27] and therefore it does not exchange readily with added thiols. Therefore, in our measurements of the surface ligands throughout the extent of the exchange, we note that the native ODPA remains on the QD surface until at high coverage of thiol, at which point thiols will start displacing ODPA. Figure 2.9 demonstrates that the ligand exchanges in our work primarily remove OA, with only ODPA removal at high thiol ligand coverages. A semi-quantitative method was employed to collect ^{31}P NMR spectra of both native QDs and ferrocene ligand exchanged QDs by using identical concentrations, as monitored by optical absorption, and identical collection parameters for the two spectra. By proton NMR, we find a 2 :1 ratio of FcC6SH to oleic acid on the exchanged QDs, indicating that significant exchange has occurred. Integration of the ^{31}P NMR peaks associated with bound ODPA show a 25% reduction in ODPA from native QDs to Fc-exchanged QDs. Therefore, the ligand exchanges presented in this paper are primarily thiols replacing oleic acid on the surface, yet residual ODPA also participates in exchange to a much smaller extent.

2.6.2 Determining the Hole Transfer Rate Constant k_{ht}

Transient absorption and transient photoluminescence are the two major spectroscopic methods of measuring rate constants. Our work predominately uses a combination of steady-state and transient fluorescence techniques to measure the relevant rate constants: k_r the radiative rate of the QD, k_{nr} the intrinsic nonradiative rate of the QD, and k_{ht} the hole transfer rate constant per molecular acceptor. With charge transfer as a viable pathway for excitated state decay, the PLQY is then related to all the rate constants by equation

2.3. While this is true for a single excited state, taken as an ensemble, it is more accurately described by equation 2.6, which incorporates the Poisson distribution to the ligand binding. The effect of the Poisson distribution is significant and should be considered in the fitting when k_r is similar to k_{ht} and at low values of $< N >$, the average number of ligands bound per quantum dot. The PLQY-N relationship with and without the Poisson factor for different limits of k_r and k_{ht} is shown in Figure 2.10. In this work, we make sure our measurements of PLQY are for $< N >$ greater than 10. Under these conditions, the two relationships yield the same PLQY and we may omit the Poisson distribution in our fitting.

$$PLQY_{avg} = \frac{k_r}{k_r + k_{nr} + Nk_{ht}} = \frac{k_r}{k_{tot}} \tag{2.5}$$

$$PLQY_{Poisson} = \sum_{n=0}^{N_{max}} \frac{N^n e^{-N}}{n!} \frac{k_r}{k_r + k_{nr} + nk_{ht}} \tag{2.6}$$

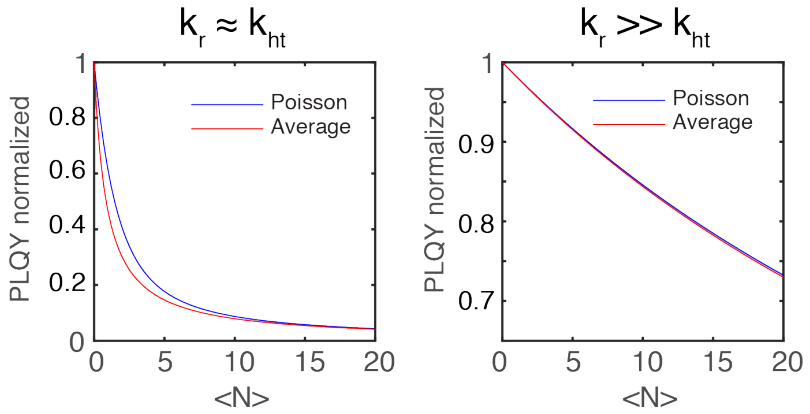

Figure 2.10: The effect of the Poisson distribution on the PLQY-N relationship

The average number of acceptor ligands bound, per QD, N, was determined by quantitative ^{1}H NMR, TEM, and ICP, similar to the number of native ligands as described in the previous section. Ferrocene has a spectrally resolved signature at 4 ppm, which was integrated against a known standard to determine the concentration of bound acceptor ligands and subsequently, N. PLQY as a function of N was plotted and fitted to equation 2.5 with known k_r, k_{nr}, N to yield the fitted parameter k_{ht}. In doing this, we asssume that k_r does not change over all the coverages of the acceptor. We demonstrate that the radiative channel is independent of the ligand exchange process in Figure 2.11b by linear relationship in plot b, where the slope should give k_r.

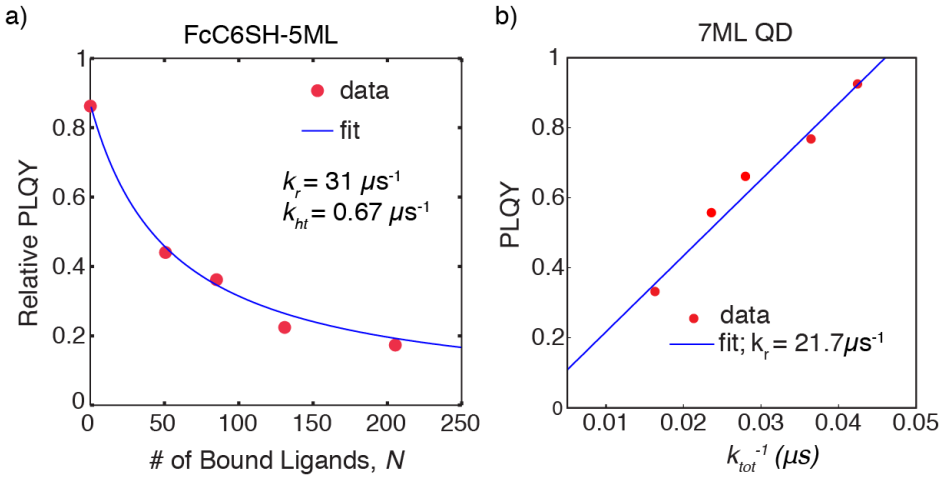

Figure 2.11: Method for determining the rate constant k_{ht}

Chapter 3

Electronic Coupling and Thermodynamic Driving Force

3.1 Electronic Coupling

In our model system, electronic coupling can be controllably tuned by varying the distance and material between the donor and acceptor. Specifically, we modulated the CdS shell thickness and the distance of the alkyl chain of the ferrocene linker. By measuring the charge transfer rate as a function of the distance dependence, we should uncover the damping coefficient β of the two materials, which is related to the height of the energy barrier of CdS and the saturated carbon chain (equation 1.2) [28].

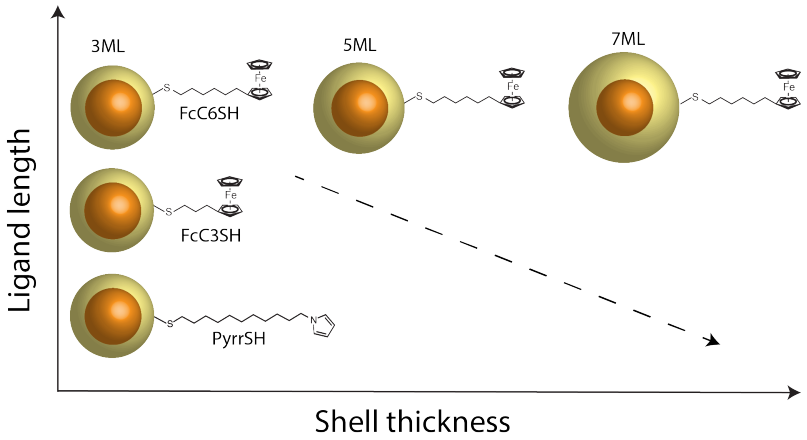

Figure 3.1: Cartoon of the nine systems with varying electronic coupling

We explored a total of nine different donor acceptor coupling systems, achieved via all permutations possible from the three shell thicknesses and three different acceptor molecules used in this study. The nine systems are depicted in Figure 3.1. We used CdSe-core with 3ML, 5ML, and 7ML CdS shells. The physical and optical properties of these three sizes of quantum dots were detailed in the last chapter. The acceptors used were ferrocene and pyrrole ligands covalently linked to the nanocrystal surface via the thiolate binding group Figure 3.3. The donor—acceptor distance is well-defined in our system, achieved by using a nearly spherical nanocrystal morphology and acceptors that contain well-characterized binding groups. This expected well-defined distance is further verified in this study, as we use two ferrocene ligands with different alkyl chain lengths, 3- ferrocenylpropanethiol

(FcC3SH) and 6-ferrocenylhexanethiol (FcC6SH), to demonstrate that the charge transfer rate constants match what would be expected for tunneling through saturated alkyl chains.

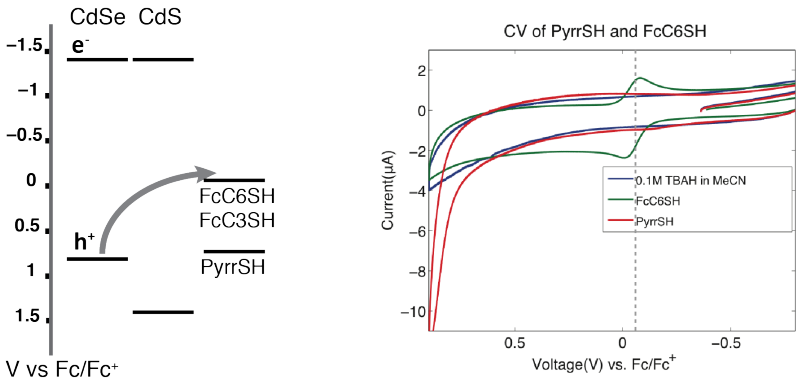

Figure 3.2: Energy levels of the charge transfer system

The energy offsets of this charge transfer reaction described in the last paragraph are depicted in Figure 3.2, and are determined via cyclic voltammetry of the acceptor molecules. Ferrocene's oxidation potential lies approximately 850 meV above the valence band of the CdSe core based on a previous measurement[29]. The large thermodynamic driving force for photoinduced hole transfer allows this process to compete with native radiative recombination. This is reflected in the measured PL[30] and PL lifetime[29]. We preclude the possibility of resonance energy transfer due to the lack of spectral overlap of the ferrocene absorption with QD emission. We also preclude electron transfer because the LUMO of ferrocene lies well above the conduction band of CdS and CdSe and is approximately 2.7 eV higher than the ferrocene HOMO position.

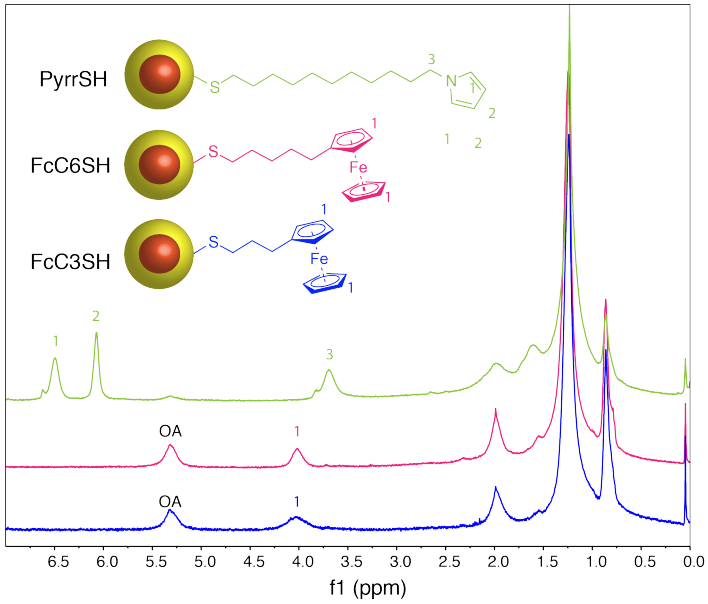

Figure 3.3: NMR of the acceptor ligands bound on the QDs

We also examine the effects of the thiolate on hole transfer by using a thiol alkyl ligand

with an NMR tag: 11-(1H-pyrrol-1-yl) undecane-1-thiol (PyrrSH). Although the pyrrole group has a 100 meV driving force for hole transfer, Figure 3.2, the 11 carbon chain distance precludes pyrrole oxidation from being a significant hole transfer pathway, as the already low rate associated with the weak driving force is now diminished completely by an exponential dropoff in the rate across such a large distance. Therefore, PyrrSH functions as a control for examining hole transfer to surface thiols, a well-known shallow hole trap for CdSe materials [31].

All ligands measured here have spectrally resolved signatures in ^{1}H NMR that allow for facile quantification. The assignments to the relevant protons of these acceptor molecules are shown in Figure 3.3. As discussed before, the signatures of molecules closer to the particle have broader lines. Indeed, the peak associated with the pyrrole protons is less broad than that of ferrocene protons of FcC6SH which is less broad than that of FcC3SH, the acceptor ligand with the acceptor molecule closest to the QD surface. The peaks are integrated with respect to a calibrated sample, and the number of bound acceptors N per QD was determined.

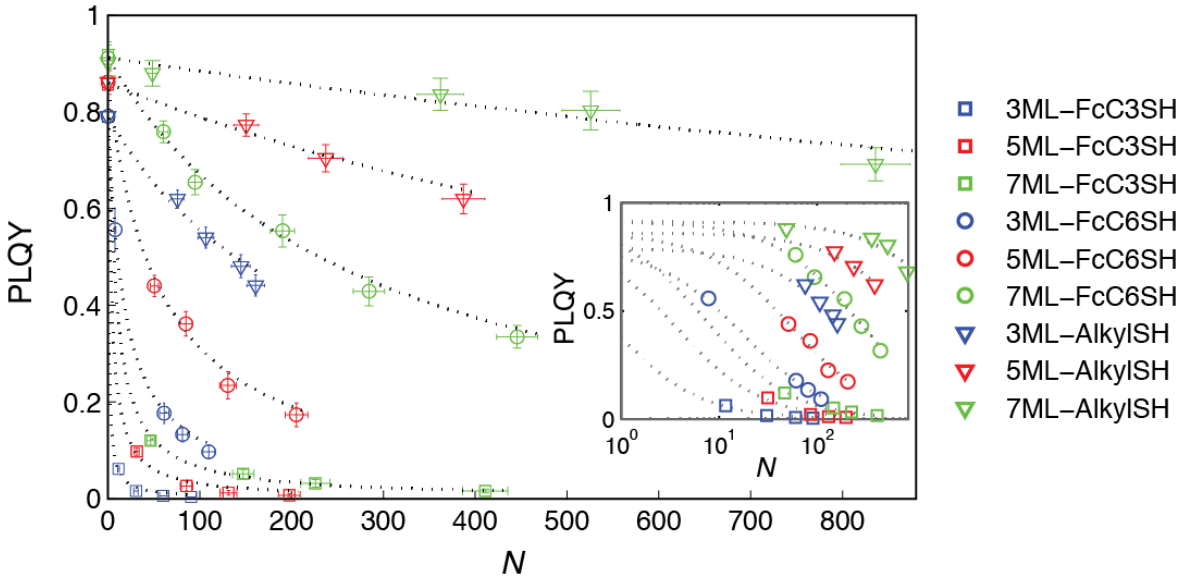

Figure 3.4: PLQY-N relationships for the nine donor-acceptor systems explored

To measure the rate constant for hole transfer, we measured the PLQY's dependence on N for each of the nine systems, discussed in the previous section. With known k_r and k_{nr} from fluorescence lifetime measurements, we fit the data to eq 2.5, to yield the hole transfer rate constant per acceptor, k_{ht}, for each system.

The raw data and their respective fits are plotted together in Figure 3.4. The same relationship plotted on a logarithmic scale for N is shown in the inset, allowing us to better visualize the expected quenching due to charge transfer for N being 1 to 10, which is significant for the systems containing FcC3SH as the acceptor. The fits in Figure 3.4 agree well with the data across the nine different systems even at high coverages, thereby confirming the validity of equation 2.5. For these systems, the presence of ODPA on the QD and the weaker packing efficiency of the ferrocene ligands relative to the native oleic acid molecules

	Donor-Acceptor	$k_{ht}(ns^{-1})$	N_{max}	$N_{max}k_{ht}(ns^{-1})$	$k_r(ns^{-1})$	$HTQY_{max}$
1a.	3ML-FcC3SH	0.063 x 10^{0}	91	5.8	0.044	99.0%
1b.	5ML-FcC3SH	0.010 x 10^{0}	197	2.0	0.031	98.2%
1c.	7ML-FcC3SH	0.026 x 10^{-1}	411	1.1	0.021	97.9%
2a.	3ML-FcC6SH	0.033 x 10^{-1}	110	0.36	0.044	86.7%
2b.	5ML-FcC6SH	0.093 x 10^{-2}	205	0.19	0.031	84.1%
2c.	7ML-FcC6SH	0.079 x 10^{-3}	446	0.035	0.021	60.5%
3a.	3ML-AlkylSH	0.028 x 10^{-2}	161	0.045	0.044	44.3%
3b.	5ML-AlkylSH	0.035 x 10^{-3}	387	0.014	0.031	27.3%
3c.	7ML-AlkylSH	0.078 x 10^{-4}	836	0.0065	0.021	22.1%

Table 3.1: All nine donor-acceptor systems investigated for electronic coupling

prevent the QD from achieving the intimate ligand interactions on the surface that may lead to cooperativity.

3.1.0.1 Family of Universal Curves

$$HTQY = \frac{Nk_{ht}}{k_r + k_{nr} + Nk_{ht}} = 1 - \frac{PLQY(N)}{PLQY(N=0)} \tag{3.1}$$

Table 3.1 tabulates the values of k_r, k_{ht}, N_{max}, $N_{max}k_{ht}$, and the maximum hole transfer quantum yield, $HTQY$ (equation 3.1) for the nine systems depicted in Figure 3.1. N_{max} is the maximum number of hole accepting ligands that were experimentally measured in the respective system, and it corresponds to approximately the maximum number of ligands that could be exchanged by mixing at room temperature. As shown in Table 3.1, N_{max} depends on the size of the QD and the length of the alkyl chain of the acceptor. $HTQY_{max}$ represents the maximum hole extraction yield achieved at the highest coverage, N_{max}. The nanocrystal systems with FcC3SH achieve $HTQY_{max}$ of 97.9% to 99% at maximum coverage. k_{ht}, the hole transfer rate constant per acceptor, on the other hand, varies from 63 μs^{-1} for hole transfer from the 3 ML QD to the FcC3SH molecule to 7.8 ms^{-1} for hole transfer from the 7 ML QD to PyrrSH.

$$r = \frac{Nk_{ht}}{k_r + k_{nr}} \tag{3.2}$$

$$PLQY(\frac{Nk_{ht}}{k_r + k_{nr}} \approx 0) = PLQY_o - PLQY_o\frac{k_{ht}}{k_r + k_{nr}}N \tag{3.3}$$

The ratio, r, relating the total hole transfer rate Nk_{ht} to the sum of the native pathways for recombination (equation 3.2) determines the curvature of each data set in Figure 3.4. This can be understood by examining the two limits of $r \ll 1$ and $r \gg 1$. The curvature depends on the range of N being examined, but since we are interested in understanding the curvature over the entire region of N ligands that the QD can accommodate, the approximation for r is done at $N = N_{max}$. In the limit of $r \ll 1$, $k_r + k_{nr}$ is the dominant pathway for the recombination of photoseparated charges, even when the maximum number of acceptors, N_{max}, is bound. This limit can be approximated by a Taylor expansion of r about 0, which

when applied to eq 3.2 produces a linear relationship between PLQY and N (eq 3.3) up to N_{max}, where $PLQY_o$ is the PLQY of the QD when no charge acceptor ligands are bound. System 3c, which is the most inefficient hole transfer system, is the closest experimental example describing this limit, in which $N_{max}k_{ht}$ is slower than k_r; the plot of its PLQY as a function of coverage in Figure 3.4 is linear. Even at over 800 acceptors bound, the total hole transfer rate is still significantly slower than the k_r of the QD. This is the system with the thickest CdS shell in our study and with the low driving force thiol acceptor. To elaborate further, for many of the nine systems, this linear regime exists when examining N up to the value that validates the r approximation. For example, system 3b would be linear up to $N = 40$, approximately one tenth of its maximal value.

In the other limit of $r \gg 1$, Nk_{ht} is larger than k_r. The inverse relationship in eq 3.2 is very steep such that small N has large effects on the PLQY. System 1a demonstrates this limit at N_{max}: the $N_{max}k_{ht}$ in this system is over 2 orders of magnitude greater than $k_r + k_{nr}$, and the curvature shown in Figure 3.4 is representative of a highly inverse relationship. In the extreme examples of this limit, a single ligand charge acceptor can quench a significant portion of the QD fluorescence ($k_{ht} \approx k_r$) or even completely quench the fluorescence ($k_{ht} \gg k_r$). In our experiments, the k_{ht} of system 1a is directly competitive with k_r. As shown in the logarithmic depiction of these relationships, one FcC3SH per QD in system 1a is predicted to quench the PLQY from 79% to 37%. In other words, a single acceptor achieves a $HTQY$ of 53%. By modulating electronic coupling we were able to experimentally and systematically characterize equation 3.2 from one limit of r to the other. The other systems in this study represent the conditions that lie in between these two limits, where k_r and $N_{max}k_{ht}$ are more comparable and the equation cannot be reduced to the simpler forms.

By demonstrating that the linear and nonlinear relationships between PL intensity and coverage can both be achieved depending on r, we resolve the root of the conflicting results on this topic in the literature, which has depicted both these trends. As shown clearly and discussed previously, the ratio r determines the degree of linearity in the PLQY$-N$ relationship. As r tends to 0, the relationship becomes linear. The myriad of linear and nonlinear observations in the literature[32, 33**?**] is a consequence of the variable systems and their respective variant parameters, k_r, k_{ht}, and N. N is especially important in these measurements; given its variability, even if the approximation in eq 5 is invalid at $N = N_{max}$, smaller values of N may be valid for eq 3.3, and therefore, measurements up to that N will produce experimental data that describes a linear relationship. In systems with very effective k_{ht} such as systems 1a and 1b, there exist no values of N that give a linear relationship. The nine relationships we have shown here demonstrate that rather than being strictly linear or nonlinear, the PL coverage relationship is a function that has continuity from one extreme to the other.

3.1.0.2 k_{ht}: Reliable Comparison Across Systems

The k_{ht} values obtained allow us to accurately investigate the effects of coupling under calibrated conditions. The distance dependence of the charge transfer rate constant is described by eq 1.2, where d is the distance of the energy barrier and β is an empirical damping coefficient that describes the extent of coupling through the barrier material. By varying the shell thickness and obtaining the resulting, we can determine β for hole transfer through

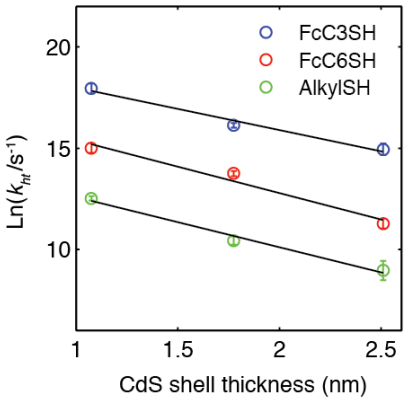

Figure 3.5: Dependence of rate on CdS shell thickness

CdS. Figure 3.5 shows the plot of the logarithm of k_{ht} as a function of the thickness of CdS for the FcC3SH, FcC6SH, and PyrrSH systems, yielding β for hole transfer of (0.22 ± 0.032) Å^{-1}, (0.26 ± 0.022) Å^{-1}, and (0.25 ± 0.021) Å^{-1}, respectively. The values are within error of each other, yielding an average of (0.24 ± 0.025) Å^{-1}, which is similar to electron transfer through conjugated carbon chains with reported β values of ∼0.2 Å^{-1} . Higher β indicates weaker coupling, or higher tunneling barrier, since the rate drops off at shorter distances. Previous work on charge transfer on semiconductor nanocrystal heterostructures has measured β of 0.91 Å^{-1} for hole transfer through ZnS in a CdSe/ZnS system [34]. This measurement differs from our system in that its hole transfer is the recombination step after electron transfer and therefore is independent of the number of acceptors. As the valence band of ZnS lies lower in energy than that of CdS, we expect the lower CdS barrier to result in higher coupling between the donor and acceptor, and hence a lower β, which agrees with the experimental results. In addition, the difference in the hole effective mass between CdS and ZnS also contributes to the lower β measured. We additionally calculated β for hole transfer through the saturated carbon bonds of the ferrocene ligand by comparing the k_{ht} for FcC3SH versus FcC6SH. This yields β of ∼(0.85 ± 0.1) Å^{-1}, which falls within what has been experimentally measured for saturated carbon chains in the literature [35]. These two β measurements together increase our confidence that the donor−acceptor distance is well-defined in our charge transfer system.

Furthermore, we can use these β values to predict the k_{ht} for hole transfer from bare CdSe QD to acceptors that are separated from the surface by a single bond. For a CdSe core with a diameter of 3.9 nm containing approximately 30 acceptor ligands, we predict a single hole transfer time constant of about 200 ps and a total hole transfer rate below 10 ps. This value is comparable to ref [36] for hole transfer from CdSe to various Ru-polypyridine complexes with similar driving force and similar donor−acceptor distance as our system. However, it is faster than the 2.5 ns rate measured for hole transfer from CdSe to phenothiazine physisorbed to the surface in a 1:1 donor−acceptor mixture,[16] which agrees with findings that electronic coupling via van der Waals forces is much weaker than those achievable through covalent interactions[12, 13].

3.1.0.3 Possible Advantages of Multiple Acceptors.

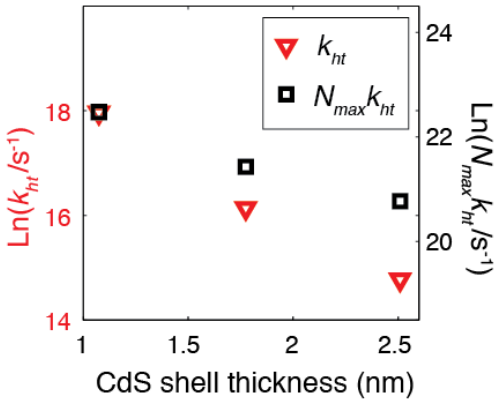

Figure 3.6: Total rate versus rate per acceptor

The QD itself is stable upon electronic excitation because one quantum of electronic excitation is distributed over thousands or even tens of thousands of atoms. When hole transfer takes place for a system with one molecular acceptor, the charge is now confined to just the atoms of the molecular acceptor. The molecular acceptor is therefore more likely to degrade by photo-degredation mechanisms before the QD does. This is the root cause of the enhanced photochemical stability of QDs over molecular chromophores. Yet by balancing rates and the number of ligands, we show that it is possible to assemble one QD with hundreds of molecular acceptors so that the degradation of one acceptor will not render the entire system inactive for further hole transfer. The ability to distribute the probability of hole transfer into many acceptors on the surface may be a strategic advantage of nanocrystal systems. Additionally, by using a molecule with a well-defined redox potential, we achieve specificity in the driving force for hole transfer. The high number of hole transfer pathways in these systems therefore provides a means by which charge transfer can occur both effectively, persistently, and specifically.

In molecular systems commonly made of a single donor and a single acceptor, the charge transfer rate k_{ct} must outcompete the native recombination pathways to be effective. For example, electron transfer from $[Ru(bpy)_3]^{2+}$ to methyl viologen is effective because the electron transfer time constant of tens of nanoseconds is much faster than the microsecond triplet lifetime of the sensitizer. Table 3.1 shows that, in the QD- molecular systems explored here, only in system 1a does the k_{ht} system reach 5.8 ns^{-1}, or a total time constant of 170 ps, which is more than 2 orders of magnitude faster than the 23 ns radiative lifetime of the QD with 3 ML shell. The $HTQY_{max}$ for this system is approximately unity. On the other hand, for six out of the nine donor—acceptor systems studied here, the k_{ht} is 1 to over 4 orders of magnitude slower than k_r. This highlights one of the important advantages of QD charge transfer as a single donor-multiple acceptor system. The addition of more acceptors can compensate for the intrinsically low k_{ht} as compared to k_r , as is the case for the systems 2a, 2b, and 2c. Although a thicker shell lowers k_{ht}, the number of acceptors that can be accommodated on this larger QD grows as the square of the radius. Therefore,

$N_{max}k_{ht}$ does not drop off by the same magnitude as k_{ht} over the same coupling distance, as shown in Figure 3.6. Additionally, k_r, the competitive pathway for charge recombination, is a tunable parameter that also affects the efficiency of hole extraction in these systems, as it approximately doubles from the 7ML QD to the 3ML QD.

To illustrate this point further, we see that system 2a has a higher k_{ht} but a lower $HTQY_{max}$ than system 1c. System 2a is more effective as a single donor-single acceptor system, with a faster k_{ht} , but system 1c is more effective as a single donor-multiple acceptor system. System 1c is able to accommodate over 3 times as many ligands as system 2a, and thus, it is able to achieve a higher total charge transfer rate $N_{max}k_{ht}$ and therefore a higher $HTQY_{max}$. Additionally, its k_r is slower than that of system 2a making it easier for hole transfer to outcompete native recombination pathways. Similarly, systems 3a and 2c depict the same trend.

	HT system	OA_o	N_{max}	Achieved Coverage(%)[1]
1a.	3ML-FcC3SH	198	91	46
1b.	5ML-FcC3SH	413	197	48
1c.	7ML-FcC3SH	890	411	46
2a.	3ML-FcC6SH	198	110	56
2b.	5ML-FcC6SH	413	205	50
2c.	7ML-FcC6SH	890	446	50
3a.	3ML-PyrrSH	198	161	81
3b.	5ML-PyrrSH	413	387	94
3c.	7ML-PyrrSH	890	836	94

Table 3.2: Summary of nine systems examined

PyrrSH is able to achieve the highest maximum coverage (Table 3.2) for the same QD size because the pyrrole group comfortably occupies the spatial volume at a distance that is 11 carbon molecules from the QD surface. On the other hand, FcC6SH with its six carbon linker and FcC3SH with its three carbon linker are more kinetically inhibited to bind at higher coverages due to the steric effects of the cyclopentadiene rings at these close distances from the QD surface. Additionally, the maximum achieved coverage is greater for FcC6SH than FcC3SH, as expected. Similar to the effects seen in modulating CdS shell thickness, a higher N_{max} afforded by the longer chain length linearly improves the total hole transfer rate $N_{max}k_{ht}$ as a result of improved packing; k_{ht} on the other hand drops exponentially over this distance due to the weaker electronic coupling at this longer chain length. Notably, the larger β (0.85 $Å^{-1}$) of the alkyl chain than that of the CdS shell (0.24 $Å^{-1}$) indicates that N_{max} achieved by modulating the chain length plays a smaller role in counteracting the effect of electronic coupling. The effect on a plot of $N_{max}k_{ht}$ in Figure 3.6 versus shell thickness will be less pronounced for the ligand shell than the inorganic CdS shell. Both $HTQY$ and k_{ht} are important in the characterization of nanocrystal charge transfer. While k_{ht} allows one to accurately compare systems as a function of variation in the parameters of charge transfer theory, $HTQY$ reflects the efficiency of the entire system to extract the hole to the surface. $HTQY_{max}$ represents the best charge transfer efficiency one can obtain from such a QD system. Therefore, the often-overlooked factors of k and N can have a significant effect on charge efficiency.

3.2 Thermodynamic Driving Force

The rate's dependence on thermodynamic driving force -ΔG on the same model system was explored to validate the existence of the Marcus inverted region.

3.2.1 Experimental Details

As discussed in the beginning of the chapter, $-\Delta G$ space was tuned by over 800 meV in energy by modification of the cyclopentadienyl rings of ferrocene with either electron donating or withdrawing groups (Figure 3.7). The electron-withdrawing group was bromine, which was found to lower the energy of the highest occupied molecular orbital (HOMO) on ferrocene by approximately 130 meV per additional bromine, in accordance with previous literature results[37]. To achieve higher HOMO energies, electron donating methyl substituents were employed. Higher HOMO energies will correspond to larger driving forces for hole transfer from the QD to the ferrocene. All the ligands were synthesized with a six-carbon linker and a thiol binding head to covalently attach to the surface of the QD. Five ligands were synthesized starting with either 1, 2, 3-tribromoferrocene (Br3Fc), 1,2-dibromoferrocene (Br2Fc), bromoferrocene (BrFc), ferrocene (Fc), or bis(tetramethylcyclopentadienyl)- iron (Me8Fc). More details about the ligand synthesis and characterizations can be found in Olshansky et al [38].

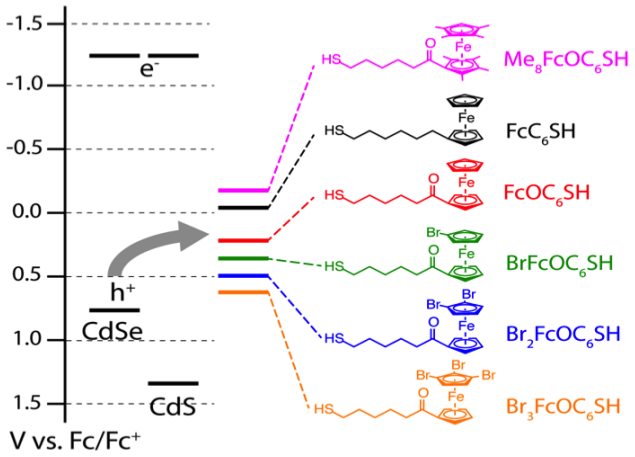

Figure 3.7: Energy diagram for hole transfer to acceptors with varying potentials

The rate constants for hole transfer were determined in the same fashion as for the electronic coupling studies. In this set of work, we maintain the electronic coupling and modulate only the driving force. The hole transfer rate's dependence on driving force was measured and plotted in 3.8, with the dashed lines being fits to the Marcus equation for reorganization energies of 400 eV to 500 eV. The data shows no Marcus inverted region, as the rates remain high at high driving force. The reorganization energy cannot be higher than what we plotted since our experiments are done in chloroform. In water, the reorganization energy of analogous ferrocene ligands is at most 0.85 eV. In the lower dielectric solvent of chloroform, this value would be decreased, and the QD would be expected to have only a minor contribution to λ.

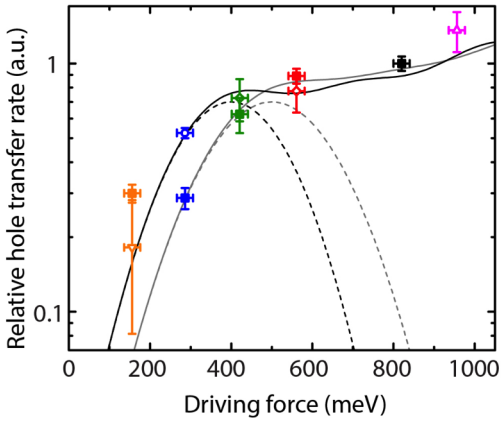

Figure 3.8: Rate dependence on Driving Force

3.2.2 Auger-Assisted Model

We turn to the recently posited Auger-assisted model for electron transfer from photoexcited QDs to better model our data[39, 40]. In this model, charge transfer can be coupled with intraband excitation of the residual charge in the QD. This allows the rate to stay high at large driving force, since the excess energy that would go to vibrations in the standard Marcus model is instead efficiently coupled into electronic excitation. Another way of understanding this is through the Marcus parabola drawings in Figure 3.9: There exists a multitude of final states, represented each by a parabola corresponding to the accessible energy levels above the conduction band given by -ΔG. As -ΔG of the lowest state moves past the intersection of the two parabolas, the rate remains high because another parabola comes into resonance with the minimum of the initial energy parabola.

The resultant rate can then be written as a sum of rates associated with each accessible electronic excitation (equation 3.4).

$$k_{ct} = \sum_{i=0} \frac{2\pi}{\hbar} |H_{ab}(E_{e,i})|^2 \frac{1}{\sqrt{4\pi\lambda k_b T}} \exp\Big(- \frac{(\lambda + \Delta G + E_{e,i})^2}{4\lambda k_b T} \Big) \tag{3.4}$$

For hole transfer, the values of $E_{e,i}$ correspond to conduction band energy levels relative to the band edge where $E_{e,0} = 0$. More information on the energies of the conduction band used in the study is detailed in [38]. This Auger-assisted model is termed "Auger" to allude to the analogous and more well-known Auger effect responsible for nonradiative recombination in systems with an extra charge.

Despite the success of the Auger-assisted model in reproducing the experimental data, there is currently no direct spectroscopic evidence for the intraband transition associated with the Auger-assisted mechanism, and other mechanisms could be proposed. For example, Auger-assisted electronic transitions within the distribution of surface states could also be coupled to charge transfer, which would also eliminate the inverted region. Further transient spectroscopic studies that can directly probe the absorption of the coupled transition would be necessary to definitively determine which state is coupled to charge transfer. There is ongoing work in the Alivisatos group to use temperature to bring out the signatures of the inverted region.

Nevertheless, the experimental trend informs avenues for designing more efficient QD-based photoconversion devices. The results suggest that the initial hole transfer process should be driven by approximately 300—500 meV (∼λ), but any additional driving force will result in minimal gains in rate. The results from this model system can also help to understand how charge trapping competes with QD luminescence, relevant for applications in QD emission. Specifically, because charge transfer rates to traps will not decrease at high driving force, QD trap states deep within the band gap would continue to be efficient quenchers of emission. Lastly, in the context of the Auger-assisted model, one would expect the Marcus inverted region to be present for hole transfer in charge separation systems in which the electron transfer occurs on faster time scales than hole transfer. In this case, hole transfer would occur with no electron in the conduction band, thus eliminating the possibility for Auger-assisted electron excitation. However, further work is needed to better resolve the underlying mechanism in order to confirm this predicted behavior.

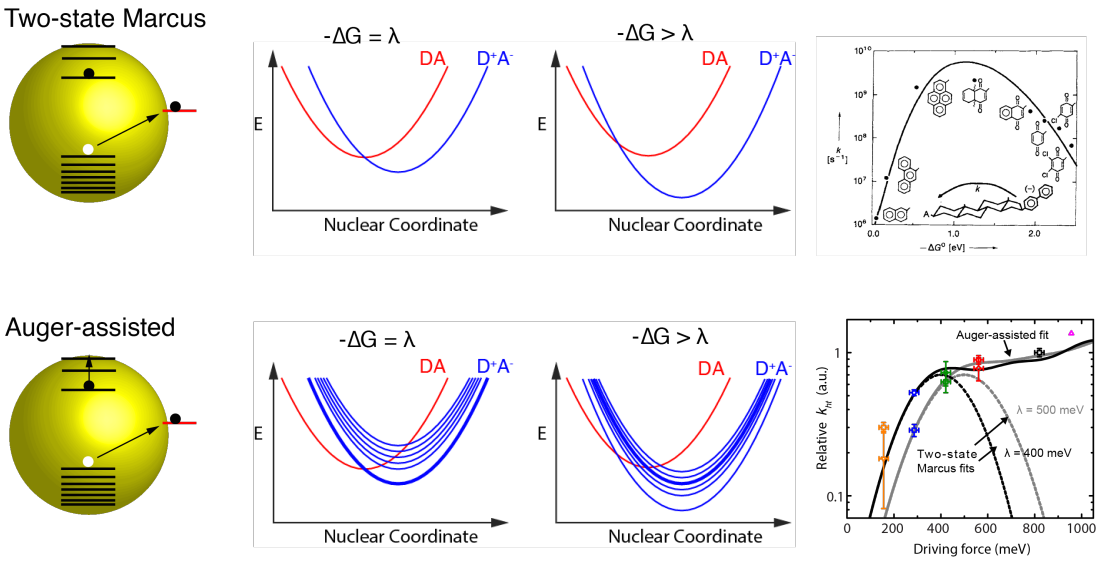

Figure 3.9: Two-state Marcus model versus the Auger-assisted model

Chapter 4

Reorganization Energy and QD's Surface Chemistry

The reorganization energy, λ, represents the energy associated with redistribution of charge of the system and its environment to accommodate the transfer of charge . Broken down to its components, it is made of an inner sphere component, λ_o, and outer sphere component, λ_i

$$\lambda = \lambda_i + \lambda_o \tag{4.1}$$

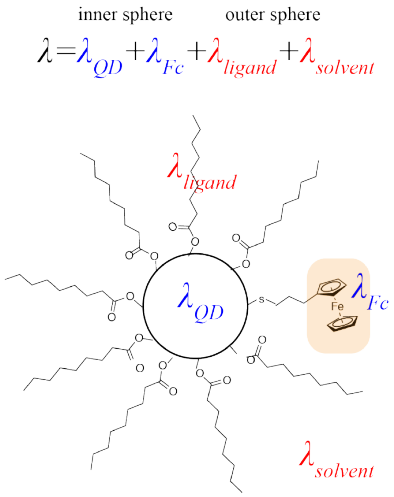

Figure 4.1: Reorganization energy

Inner sphere λ includes contributions from ferrocene and the quantum dot while the outer sphere includes the ligand environment that surrounds the ferrocene and the solvent (Figure 4.1). For a QD–molecular acceptor complex, λ_i has small contributions from the QD; computational values of this in literature vary from less than 10 meV [41] to almost 50 meV [29]. Computational values of the inner sphere molecular reorganization energy are typically a few hundred meV [42]. The value for Fc has been calculated to be 139 meV [29]. The total inner sphere reorganization here amounts to less than 200 meV.

The outer sphere solvent reorganization energy is classically estimated using a dielectric continuum model as given by equation 4.2.

$$\lambda_{solv} = \frac{e^2}{4\pi\varepsilon_o}\left(\frac{1}{\varepsilon_{op}} - \frac{1}{\varepsilon_s}\right)\left(\frac{1}{d_D} + \frac{1}{d_A} - \frac{1}{r_{DA}}\right) \tag{4.2}$$

ε_{op} and ε_s are the optical and static dielectric constant, respectively, associated with the high frequency (occuring at the speed of electron relaxation) and low frequency (associated with vibrational relaxation) limits. For a common solvent like chloroform, $\varepsilon_{op} = 2.08$ and $\varepsilon_s = 4.81$. Calculated values based on equation 4.2 give about 348 meV for charge transfer in chloroform. In the driving force studies in Chapter 3, we approximated that the total reorganization energy cannot exceed 600 meV.

However, our system is different than most molecular charge transfer studies in that our ferrocenes, being typically 6 carbons in length from the QD surface are engulfed primarily by saturated carbons (usually 18 carbons in length) in its vicinity. Investigations of a modified dieletric model are under way, where both the ligand environment and the solvent will play important roles. It is worth noting that in the self assembled monolayer literature, reorganization energy increases with chain length [43, 44].

This outer sphere reorganization energy that considers both the solvent and the ligands will depend on the packing of the surrounding ligands. The penetration of the solvent into the ligand layer also depends on this packing, which itself depends on the chemical structure of the ligand and the size of each facet [45].

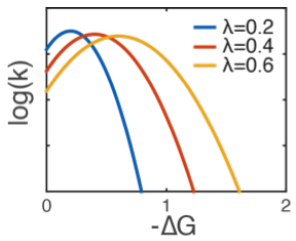

Figure 4.2: Charge transfer's dependence on λ

Experimental verification of the contributions of the ligand shell and the solvent to λ would enable us to gain tunability over λ, which is especially important in real charge transfer reactions. Figure 4.2 (assuming a two-state Marcus model) shows how a system with the lowest λ can afford the fastest rate at the smallest $-\Delta G$. In exemplary systems in literature, low reorganization energy medium like proteins act to protect the charge center from the higher reorganization energy of the solvent to produce a high reaction rate [46]. Therefore, building an understanding of the weighted contributions to the total λ in the complex QD system would be extremely useful. To begin to build this understanding, we must first try to understand the properties of the surface ligands on the QD.

4.1 Physical Characterization of the Surface Ligand Structure

In the last five years, there has been a growing body of work that focuses on understanding the surface ligands of quantum dots. What type of ligand binding motifs do they exhibit? What is the packing density? Packing order? What are their dynamics? Building

this understanding enables one to design effective ligand exchange reactions[47, 48], control solubility [49, 50], and have greater control over the material's optical properties[48].

Asaph et al. in two papers [45, 51] predicted an order-disorder phase transition of the ODPA ligands on wurtzite rod structures with facet length of 5 nm in hexanes at temperatures around 40 °C. This transition temperature shifts depending on the packing density, which depends on the length scale of the facet, the chemical nature of the ligands, the density of the ligand, and the solvent. In the ordered state, the solvent penetration is also very different than the disordered state.

Yang et al. also in two papers [49, 50] have investigated an indirect effect of this ordering phenomenon via solubility. Using saturated carbon ligands, the authors find that the solubility of QDs are orders of magnitude worse than that of QDs with "entropic" ligands, ligands with more branched structures that have lower packing order. The precipitation of QDs from this low solubility corroborates with the theoretical findings in Asaph et al. In their calculations, the repulsive forces between the particles become attractive when the ligands become ordered. This attractive force causes aggregation of the particles because their ligands have less interactive energies with the solvent, leading to particle aggregation and precipitation.

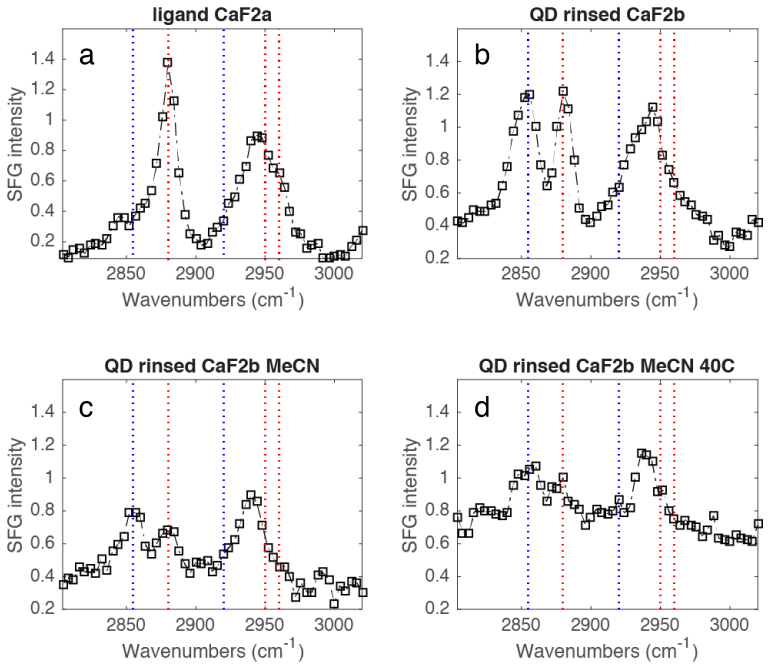

Figure 4.3: SFG on QD surface ligands. See text for vibrational mode assignments

We have collaborated with Gabor Somorjai's research group at UC Berkeley to use Sum Frequency Generation Spectroscopy to directly measure this ordering effect. The surface sensitivity to molecular conformation changes the signal intensity of CH_2 and CH_3 IR stretches. Previous work using SFG on Au nanoparticles and quantum dots show a dependence from a disordered configuration at small sizes to a more aligned (ligands lying normal to the surface) orientation at larger sizes. The surface sensitivity of SFG makes it an effective technique that can directly measure this effect [52, 53].

Figure 4.3 shows the SFG data on 7 nm CdSe-core CdS-shell particles with ODPA ligands in the CH_2 and CH_3 stretches region. The assignments are CH_2 symmetric stretch (d^+) at 2855 cm^{-1}, CH_2 antisymmetric stretch (d^-) at 2918 cm^{-1}, CH_3 symmetric stretch (r^+) at 2881 cm^{-1}, and CH_3 asymmetric out-of-plane stretch (r^-) at 2950 cm^{-1}. A weaker band at 2935 cm^{-1} is assigned to the Fermi resonance between CH_3 symmetric stretch and bend overtone modes.

The ratio of s-CH_3/s-CH_2 stretch is an indicator of the degree of order in these materials. Due to the configurational sensitivity of SFG, molecules oriented perpendicular to the face of the particle should exhibit a strong CH_3 signal that has no inversion symmetry, but weak CH_2 stretches since all trans conformation should effectively cancel one another because of the approximate inversion symmetry. Gauche defects in which the ligands bend will result in the CH_2 stretch modes at the defect position becoming "SFG-allowed" [54].

In our data in Figure 4.3, we can see that free ligands (ODPA) themselves orient in an ordered configuration on CaF_2 substrates. On QDs (after rinsing off any residual free ligands), their degree of order decreases, but remains high at room temperature. We then attempted to determine the dependence on the ratio of s-CH_3/s-CH_2 as temperature increases. We seek to experimentally measure this phase transition by detecting a marked charge in the ratio of s-CH_3/s-CH_2 over a small temperature range. We hope better design of the cell chamber that allow the use of organic solvents and temperature modulation would lead to these insightful experiments. Better control over the ligand density would also improve the sharpness of these order disorder signatures.

4.2 Kinetics of Ligand Exchange

Due to their high surface area to volume ratio, QDs can have highly variable optical and electronic properties that strongly depend on their surface ligands. However, little research has been done to address the basic kinetics and thermodynamics of ligand binding and exchange. This work attempts to fill in these fundamental gaps that are of ubiquitous importance in QD applications. In the previous chapter, we have shown the upper and lower bounds of the hole transfer rate in QD donor acceptor systems by measuring PLQY as a function of the number of bound charge acceptor ligands, N. Here, we use the same system to probe the kinetics of ligand binding. In the limits where one ligand causes a distinguishable change in the PLQY, we are able to study the kinetics of low binding events, which has almost no precedence in literature. System 1a, CdSe-core with 3ML CdS shell with FcC3SH acceptor from Table 3.2 has the fast k_{ht} necessary to allow photoluminescence to be a direct proxy for quantitative binding of the first few acceptor ligands. One Fc ligand drops the QD PL down by over 50%.

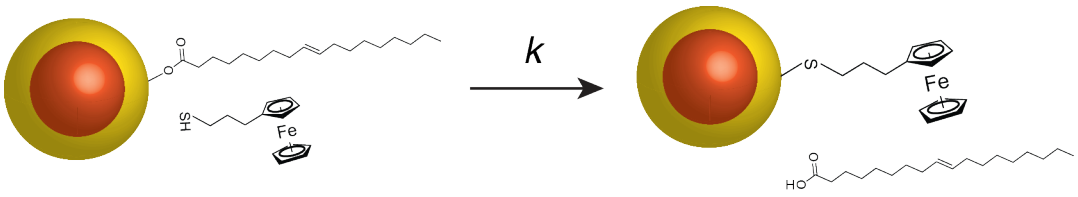

Figure 4.4: Ligand Exchange being investigated

The ligand exchange under investigation is depicted in Figure 4.4, the same thiol exchange for native oleic acid as in our previous work. In Chapter 2, we characterized N at larger than 10 to gain an understanding of the k_{ht}. Here, we are investigating the low limit of N where the Poisson distribution must be implemented for accurate fitting to the PLQY equation. Furthermore, in this limit ($<N>$ less than five), we may assume that the thiol ligands we add readily displace the native oleic acid to achieve full exchange. At high binding, this assumption breaks down as the packing of the bulky ferrocene and the limited number of sites will prevent the system from reaching full exchange. Experimentally, we employ the same methods as described in Chapter 2 to determine the k_r, k_{nr}, and k_{ht}. Figure 4.5 depicts the PLQY's relationship to N with and without the Poisson factor for an example QD charge transfer system used in these studies, overlaid with experimental data collected. This shows that the low binding regime data collected agrees well with the Poisson model of ligand binding.

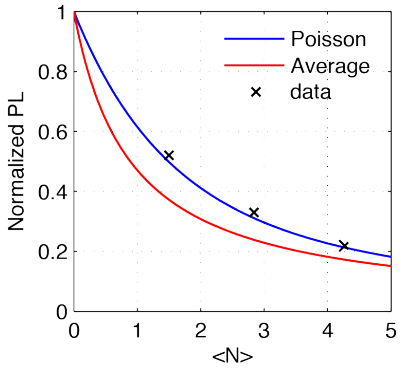

Figure 4.5: Poisson relationship is valid for low binding events

4.2.1 Proposed Model of Ligand Exchange

We collect our kinetics data using stopped-flow fluorescence spectroscopy (Applied Photophysics SX20). CdSe-core CdS-shell (typically 3-4 ML) particles in various organic solvents are mixed at very fast timescales with known concentrations of FcC3SH dissolved in the same solvent. The dead time for our experiments is less than 1 ms, allowing us to monitor PL intensity in the millisecond to seconds timescales. The sample chamber is excited by monochromatic 500 nm light from a Xe lamp and only photons associated with the PL (filtered by a 560 nm bandpass filter) were collected by a PMT detector. Raw PL data is shown in Figure 4.6a. Using the $PLQY - N$ relationship for that given charge transfer system, we can convert the data to $<N>$ as a function of time (Figure 4.6c). The slopes at the early times (Figure 4.6b) give us the reaction rate ∂ <N>$/\partial$ t. Examining this reaction rate as a function of different concentrations of ligand [FcSH], we can determine the rate law, rate constant, the order, and explore the mechanism of the ligand exchange reaction. A proposed rate law is given by equation 4.3.

$$\frac{\partial < N >}{\partial t} = \frac{1}{[QD]} \frac{\partial [^*FcSH]}{dt} = \frac{1}{[QD]} \frac{-\partial [FcSH]}{\partial t} = k[^*OA][FcSH] \tag{4.3}$$

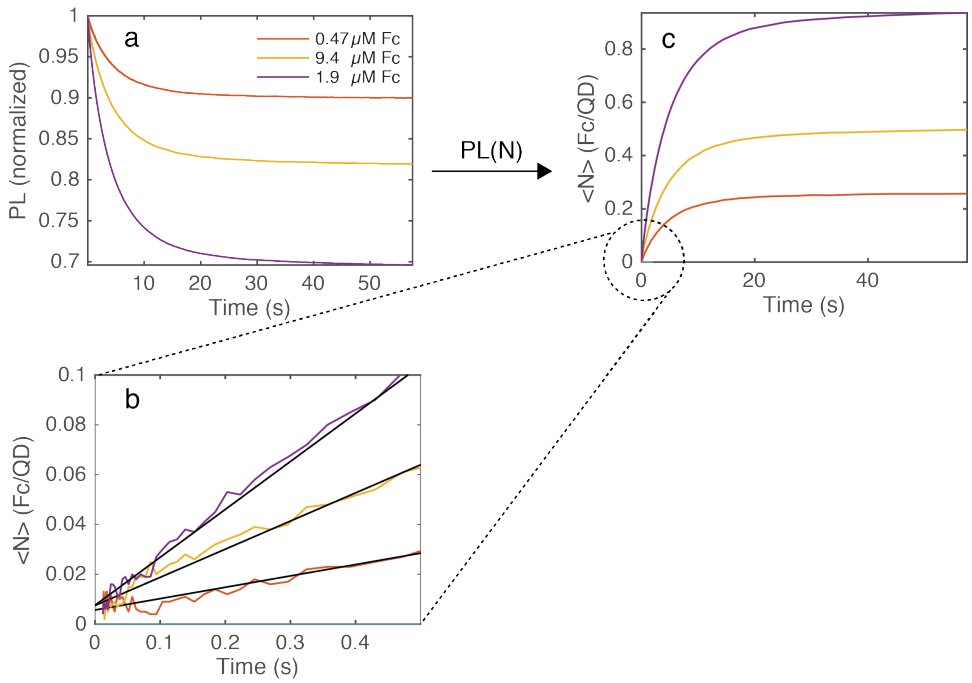

Figure 4.6: Raw data on PL and $<N>$ as a function of time

where $[^*OA]$ is the concentration of oleic acid ligands on the QD surface. These are the available sites for ligand exchange.

We implement pseudo first order approximation to our reaction, since $[^*OA] \gg [FcSH]$. In the low binding limits of our work, the concentration of FcC3SH is about two orders of magnitude less than the native oleic acid concentration on the QD surface. This means that, relatively $[^*OA]$ is unchanged throughout the course of the reaction and can be treated as a constant.

e

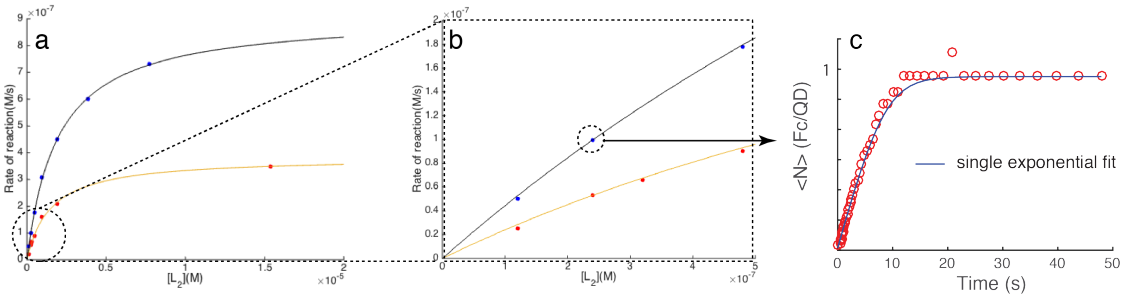

Figure 4.7: First derivative reaction rate as a function of FcC3SH.

Varying [FcSH] and measuring the initial rate ∂<N>/ ∂T. in Figure 4.6b, we find that the rate law is first order with respect to [FcSH] at low concentrations. At higher concentrations of [FcSH], we see that the rate increases at less than the linear relationship, likely due to the more appropriate Langmuir Hinshelwood mechanism that considers a surface reaction model. Langmuir Hinshelwood model is often used for bimolecular chemical reactions like

heterogeneous catalysis occuring on a surface [55, 56]. The model is adapted from the Langmuir model of reversible adsorption of molecules on solid surfaces. The Langmuir Hinshelwood model rate law for this reaction is shown in equation 4.4.

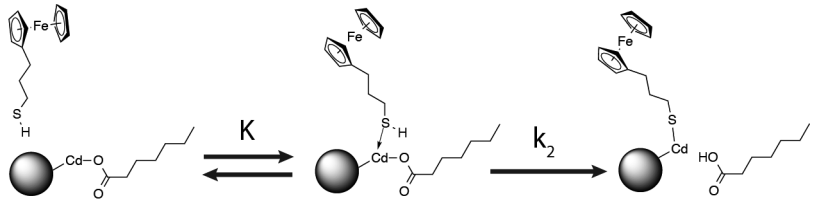

Figure 4.8: Two-step binding model

$$\frac{\partial < N >}{\partial t} = \frac{1}{[QD]} \frac{-\partial [FcSH]}{\partial t} = \frac{k_2 K [^*OA][FcSH]}{1 + K[FcSH]} \tag{4.4}$$

In the limit that $K[FcSH] \ll 1$, the reaction rate simplifies to the linear relationship first presented.

$$\frac{\partial < N >}{\partial t} = \frac{1}{[QD]} \frac{-\partial [FcSH]}{\partial t} = k_2 K [^*OA][FcSH] \tag{4.5}$$

In this model, there is a fast equilibrium step that precedes a nonreversible rate-limiting step. Applying this model to our ligand exchange reaction, we believe that the equilibrium step is the thiol first coordinating datively to the surface cadmium sites without any proton exchange. The rate limiting step is the proton transfer from the thiol to the carboxylate, thereby resulting in a thiolate bond with Cd and a free carboxylic acid molecule. This mechanism has been suggested by Hens et al to explain different timescales seen in NMR spectroscopy, and is pictorally presented in Figure 4.8 [57].

Our preliminary data, which fits well to this model (Figure 4.7), corroborates this mechanism. In Figure 4.7a, the data is fit to the Langmuir Hinshelwood rate law. Figure 4.7b shows the zoomed in linear region at low concentration. We see the data move away from this linear relationship at higher concentrations of added ligands. In the limit where the rate scales linearly, we can fit the raw data to a single exponential (Figure 4.7c) and obtain the observed rate constant $k_{obs}$where $k_{obs} = k_2 K[^*OA]$. The quantitative data are tabulated in Table 4.1.

4.2.2 Competitive Binding

$$\frac{\partial < N >}{\partial t} = \frac{1}{[QD]} \frac{-\partial [FcSH]}{\partial t} = k_{obs} = \frac{k_2 K [*OA][FcSH]}{1 + K[FcSH] + K2[RNH_2]} \tag{4.6}$$

To verify the validity of this two step model, we added a competitive reversible binder, an alkyl amine, which has been shown to datively coordinate to surface Cd through L type binding motifs, an important property that helps break up Cd-ODPA or Cd-Oleate polymers that form in solution [58]. No proton exchange occurs for these ligand interactions so it would simply compete with the equilibrium step in 4.8 and not lead to any differences in

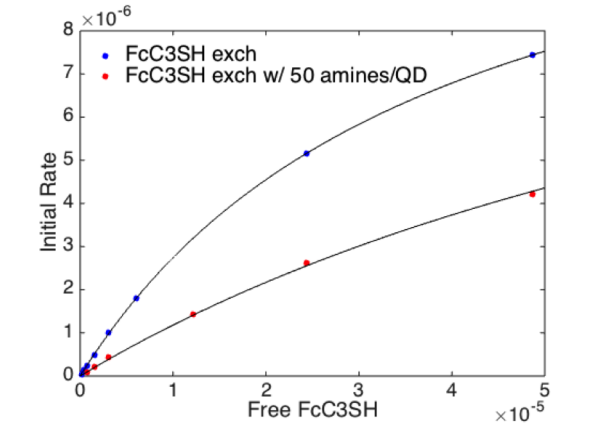

Figure 4.9: Competitive binding data

final thermodynamic state of bound ferrocene acceptors per QD. We examined the observed reaction rate and fit the data (Figure 4.9) to the rate law obtained from this competitive binding model as shown in equation 4.6, using k_2 and K determined from the non-competitive case.

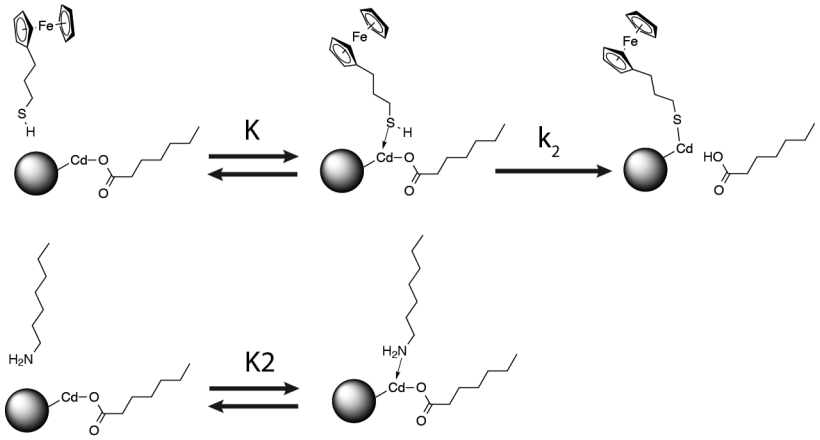

Figure 4.10: Competitive model

Using this competitive binder, we can determine the equilibrium constant $K2$ of the amine dynamics on the QD surface, which is documented in Table 4.1.

4.2.3 The Effect of Surface Ligands on the Binding Rate

As discussed earlier in the chapter, the surface of these QDs can have different physical structures, from an ordered geometry where the van der Waals interactions between the ligands are high to a disordered state where instead the ligand entropy is high, leading to better dispersity in solution. We changed the surface ligands of QDs to examine how that affects the rate constant k_{obs}. We find that changing from oleic acid to nine carbon (nonanoic acid) and 18 carbon (stearic acid) saturated carboxylic acid chains results in slower k_{obs}. The

interesting observation is that the length of the chain does not affect the rate constant, as nonanoic acid and stearic acid yielded the same k_{obs}within error. However, both systems are slower by a factor of around two than QD's with native oleic acid. Oleic acid has a characteristic cis double bond at carbon number 9, resulting in a kink in the chemical structure of the molecule. We believe this kink causes the disorder effect in the ligand structure, resulting in better penetration of the solute into the ligand shell and subsequently the surface of the quantum dot where the ligand exchange reaction must take place. These results corroborate with other ongoing work in our research group on the thermodynamics of ligand exchange, which also shows a high ligand to ligand interaction in straight chain ligands versus oleic acids.

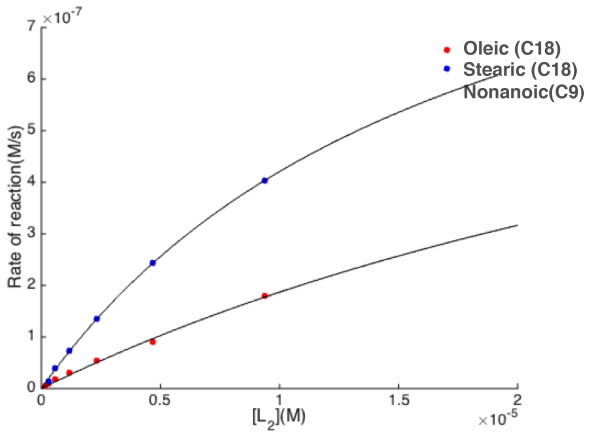

Figure 4.11: Rate data for QDs with different native ligands

	s^{-1}	K (M^{-1})	K2 (M^{-1})
C18 Oleic	0.01	2 x 10^4	NA
C18 Stearic	0.008	9 x 10^3	NA
C9 NonAnoic	0.008	9 x 10^3	NA
C18 Oleic+Amine	0.01	2 x 10^4	5.6 x 10^4

Table 4.1: Rate constants for kinetics of ligand binding

This compilation of preliminary data we have collected shows that the rate of ligand binding shows strong dependence to the native organic makeup and structure of the QD. In the presence of dynamic on and off adsorption species, the rate constant of our desirable reaction decreases due to a decrease in the number of available sites to bind to at a given time. Using this FcC3SH ligand exchange for native carboxylate, we have introduced a quantifiable and reliable method to probe the structure of the organic surface of the QD, as well as the thermodynamics along the reaction coordinate diagram.

Chapter 5

Single Particle Photophysics: Photothermal and Fluorescence Microscopy

5.1 Single QD Photophysics

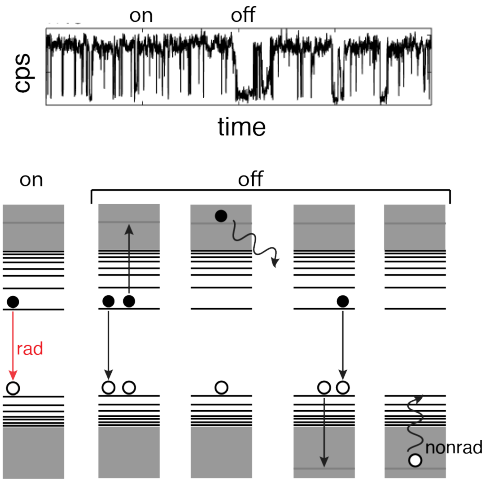

Figure 5.1: Auger Recombination in QD

Studies of QDs at the single particle level reveal new insights into the photophysics of the material not detectable via the same measurement on the ensemble scale, due to the blurring out of these features when averaged across a large sample size. Examples of these unique single particle features include fluorescence intermittency [59], bimodal distributions of the optical properties of QDs [60], and subpopulation of particles that exhibit no fluorescence [61].

Single QD photophysics studies are dominated by fluorescence microscopy, where technology like electron-multiplier CCD and avalanche photodiodes paved the way for routine detection of single molecules and particles in tens of millisecond timescales. Using fluorescence microscopy, fluorescence intermittency, or blinking, has dominated as a topic of contentious debate for the last twenty years. Blinking is the fluctuation of on and off states in a single QD's PL, which most of the community have attributed to Auger recombination. Most of the work done in this area is focused on verifying the origin of this blinking mechanism, by determining the on and off coefficients of the power law relationships.

Fluorescence is the tool of choice for single molecule and particle characterization because it is a background-free technique. Molecular dyes and quantum dots exhibit similar fluorescence intensity trajectories, yet the mechanisms by which they exhibit their on and off states are fundamentally very different. In molecular dye blinking, the photoexcited electron transfers to a triplet state, which has a long lifetime. During this time, absorption cannot occur until the triplet state relaxes [62]. Therefore, fluorescence turns off in a blinking trace due to lack of absorption.

In QDs, it is via Auger recombination, the mechanism depicted in Figure 5.1. In this process, two excitons are formed inside the particle. One pair recombine in the form of energy transfer to one of the charges of the residual exciton. The charge is ejected to the surface, leaving a residual charge inside the nanocrystal that is relatively decoupled from the surface charge. Further excitons formed in the material will transfer their energies to exciting the residual charge to a higher energy state, from which it relaxes nonradiatively. This causes the 'off' state of the blinking behavior, in which no photons are emitted. Eventually, the residual charge recombines with the surface charge, and photoluminescence ('on' state) can continue. In QDs, fluorescence turns off in a blinking trace due to lack of fluorescence.

Although the fluorescence trajectory of molecules and quantum dots both exhibit these similar on and off states, we expect the nonradiative heat emission channel to be different since the origins of these fluctuations in fluorescence can be due to lack of absorption for molecules versus lack of fluorescence for QDs. The predicted correlation between the thermal emission and fluorescence is shown in Figure 5.2. In molecular dyes, since there is no absorption, there is no fluorescence or emission. In QDs since absorption persists, the photons for fluorescence is converted to heat emission during an off state.

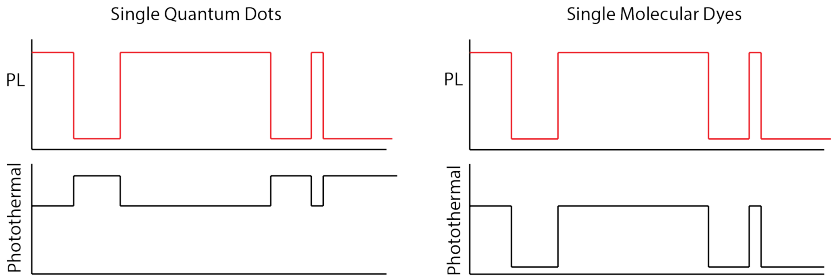

Figure 5.2: Predicted correlation between thermal and fluorescence intensity of single quantum dots and single molecular dyes.

Three events dictate an absorber's steady-state optical properties: absorption, radiative emission, and nonradiative thermal relaxation. A handle on two of these three parameters elucidates much more information about the absorber's photophysical properties, such as its quantum yield. Currently, the quantum yields of single absorbers are difficult to measure because only fluorescence can be measured. For example, higher PL may either indicate higher PLQY or higher absorption coefficient. Besides being able to examine the PLQY distribution of a given sample, being able to measure the absorption and fluorescence simultaneously would allow us to at long last, resolve some of these contentious photophysical mechansims governing single molecules and single quantum dots. Thus, our efforts will first focus on developing a new method for measuring the absorption of single QDs.

5.2 Photothermal Prospects and Limitations

Although the single molecule detection was first demonstrated in absorption mode, fluorescence microscopy has instead become the ubiquitous method of choice in detecting single objects for two main reasons: it is background-free and relatively simple to implement. Absorption is an inherently more common and robust process than fluorescence, and it is less sensitive to the environment. However, the detection of absorption via the common method of transmission is at least 10^3 times weaker in sensitivity than fluorescence [63]. The challenges for observing absorption are further exacerbated when reduced to a single molecule. First, the attenuation of a laser beam by a single molecule is 10^{-7}, much smaller than typical laser fluctuations. Second, the molecule's absorption cross section is one-millionth the area of the narrowest visible beam, meaning the background signal is overwhelming. Traditionally, these challenges were addressed by operating at cryogenic conditions, embedding the molecules in a crystal matrix that acts to spectrally scatter the molecules, and combining a series of lock-in detection techniques.

The past decade has seen many successful efforts to detect single-molecule absorption at room temperature. Photothermal microscopy, a thermo-optical technique that detects non- radiative emission, was the first to do so[64]. A series of papers by Sandoghar and colleagues demonstrated the detection of single- molecule absorption via transmission by using a sophisticated method to reduce laser fluctuations and background[65, 66]. In a study by the Xie group, two double-modulated excitation beams were used to detect the depletion of the ground absorption state of the molecule [67]. Despite this progress, the excitation flux used in all of the mentioned work is 100—1000 times higher than that used in routine single-molecule fluorescence microscopy. Under these conditions, nonequilibrium processes arise, such as triplet— triplet annihilation in molecules[68] and Auger recombination in semiconductor materials[69]. The population of these unstable energy states increases the pathways for chemical photodegradation of the absorber, rendering it unstable for measurement times longer than tens of seconds[64]. In order to study molecules and particles under steady-state conditions for a prolonged period of time, it is essential to improve the sensitivity of absorption microscopy which would allow us to lower the heating powers used.

Out of all the room-temperature absorption techniques discussed, photothermal microscopy is the most extensively studied, and its theoretical understanding is the most established because of its similarity to other photothermal spectroscopy methods that were studied decades prior[70]. In this technique, a frequency-modulated heating beam photoexcites the absorber, which releases heat to the surrounding medium via nonradiative relaxation pathways. This heat results in a temperature increase in the region around the absorber, which induces a temporally and spatially varying refractive index change Δn (5.1). The time-dependent temperature profile in the steady-state regime (eq 5.2) depends on the important parameters of thermal conductivity (κ), radial distance (r) from the center of the absorber, intensity of the excitation beam (I_{heat}), the absorber's absorption cross section (σ), and thermal diffusion length (r) of the dissipated heat, which is given by eq 5.3 and depends on the modulation frequency (Ω), isobaric heat capacity (C_p), and κ.

$$\Delta n(r,t) = \frac{\partial n}{\partial T}\Delta T(r,t) \tag{5.1}$$

$$\Delta T(r,t) = \frac{I_{heat}\sigma_{abs}}{4\pi\kappa r}[1 + \exp(-r/r_{th})\cos(\Omega t - r/r_{th})] \tag{5.2}$$

$$r_{th} = \sqrt{\frac{2\kappa}{\Omega C_p}} \tag{5.3}$$

In the experimental setup for photothermal microscopy, a probe beam with wavelength outside the absorption window of the particle is focused at the same volume as the heating beam and scattered by the medium's Δn at the same frequency as the heating modulation. The signals are fed into a photodetector, and the component associated with the input frequency is extracted via a lock-in amplifier. The measured signal therefore depends on the overlap of the probe beam with the volume of thermal dissipation. Specifically, r_{th} should be close to the radius of the probe beam (ω) to obtain the maximal signal detection. Because ω is known for a given wavelength, we can determine the characteristic time constant for thermal relaxation τ (eq 5.4). Choosing a modulation Ω such that $\Omega\tau \approx 1$, with

$$\tau = \frac{\omega^2 C_p}{2\kappa} \tag{5.4}$$

we ensure that the probe beam focus is matched to the region where the temperature is effectively modulated. The interaction of the probe beam with Δn has been previously modeled [69]. The results produce a relationship for the photothermal signal-to-noise ratio (SNR) (eq 5.5), where f(Ω) is a function that describes the complex frequency dependence of the signal, which is strongly dependent on r_{th}.

$$SNR = \frac{1}{\pi\omega\lambda^2\Omega} n \frac{\partial n}{\partial T} \frac{1}{C_p} \frac{\sigma_{abs}}{A} P_{heat} \sqrt{\frac{P_{probe}\Delta t}{h\nu}} \tag{5.5}$$

5.3 Exploitation of Critical Point Divergence of Xe to Enhance SNR

To enhance photothermal sensitivity, we exploit the divergent behavior of the thermal expansion coefficient of Xe, α_p, proportional to $\partial\rho/\partial$T (eq 6; ρ is density). This coefficient's divergence is a fundamental thermodynamic phenomenon of second-order phase transitions in fluids. Given density's close relationship with refractive index, n, the thermo-optical parameter $\partial n/\partial$T in eq 5.5 also diverges under these conditions, giving rise to the well-known critical opalescence. One can take advantage of this divergence by conducting photothermal microscopy in solvents near the critical point, where ∂n/∂T is extremely large. Three groups have sought these strategies by exploring photothermal signal enhancement near the thermotropic phase transition of 4-cyano-4´-pentylbiphenyl (5CB) liquid crystals. They measured about a 20-fold signal enhancement factor in this medium over glycerol[71, 72, 73]. Liquid—vapor phase transitions are sharper and therefore have larger ∂n/∂T than thermotropic phase transitions. Past work in photothermal deflection spectroscopy, a bulk photothermal technique that abides by the same thermo-optical concept, using supercritical fluids CO_2 and Xe as solvents enhanced the photothermal signal by a factor of 100—1000[74, 75]. In this chapter, we demonstrate this concept for photothermal microscopy by experimentally

measuring the signal of single Au nanoparticles (NPs) near the critical point of Xe (T_c = 16.583 °C, P_c = 5.842 MPa).

5.3.1 Theoretical Predictions

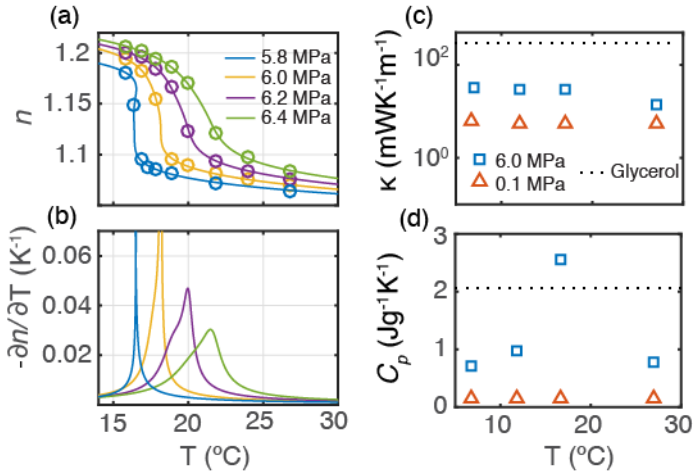

Figure 5.3: Theoretical predictions of thermodynamic parameters of Xe

To predict the photothermal signal response to conditions near the critical point, we have compiled thermodynamic values of density, temperature, pressure, C_p, and κ for Xe at standard temperature and pressure (STP) to near critical point from past literature [76, 77, 78]. We present the divergence of α, C_p, and κ in informative plots in Figure 5.3. Complementary to Figure 5.3 is Table 5.2, which compares the values of the thermodynamic parameters relevant in this chapter for STP Xe, critical Xe, and glycerol. The refractive index, n, was related to density via the Lorentz—Lorenz relationship, using the reported Lorentz— Lorenz parameter of 10.5 cm^3/mol for the range of temperatures and pressures investigated in this study[79]. The thermo-optical relationship between n and temperature for Xe is then illustrated in Figure 5.3a, which resembles the pressure—density—temperature surface in the vicinity of the critical point. From the figure, we also see that n of Xe approaches a maximum value of 1.2 at our thermodynamic operating range, which is a larger index mismatch with glass than glycerol (n = 1.47). From the fitted data in Figure 5.3a, we can obtain $\partial n/\ \partial$T for this same region, shown in Figure 5.3b. As conditions tend to the critical point, the values of ∂n/∂T become not only larger but also more sensitive to small changes in temperature and pressure, as depicted by the narrow temperature width of $\partial n/\ \partial$T at 5.8 MPa.

The dependences of C_p and κ on temperature and pressure, which also affect the photothermal SNR (eq5.5), are shown in Figure 5.3c,d. Divergence of C_p and κ are theoretically predicted at the critical point [80]. However, because of sparse existing experimental data on C_p and κ near the critical point of Xe [76] and the different critical exponents of C_p and κ [81, 82], the divergence is not clearly evident from Figure 5.3 c,d. We further note that conditions below the critical point might appear to lead to a high photothermal signal because of the density discontinuity across the gas—liquid coexistence (saturation) curve.

	units	glycerol	Xe_{STP}	Xe_{crit}
n		1.473	1	1.138
κ	$mW \cdot m^{-1} \cdot K^{-1}$	290	5.4	28.9
C_p	$J \cdot g^{-1} \cdot K^{-1}$	2.06	0.16	2.55
$\lvert\partial n/\partial T\rvert$	K^{-1}	2.7 x 10^{-4}	5 x 10^{-6}	$\sim$ 4 x 10^{-2}

Table 5.1: Thermodynamic parameters

However, the creation of bubbles across a gas—liquid interface requires large excess heating and a nucleation process that is highly nonlinear and difficult to control.We therefore limit our discussion to near critical states that have high but continuous $\partial n/\ \partial$T.

5.3.2 Experimental Setup

Xenon was chosen for its relatively achievable critical pressure and temperature compared to other common gases and for its relatively low $\varkappa$ and C_p [75]. For example, Xe has κ and C_p values that are more than 10-fold lower than those of CO_2, another chemical with critical point near that of Xe. Equations 2 and 5 indicate that lower values of C_p and κ generally improve the photothermal signal and therefore are desirable.

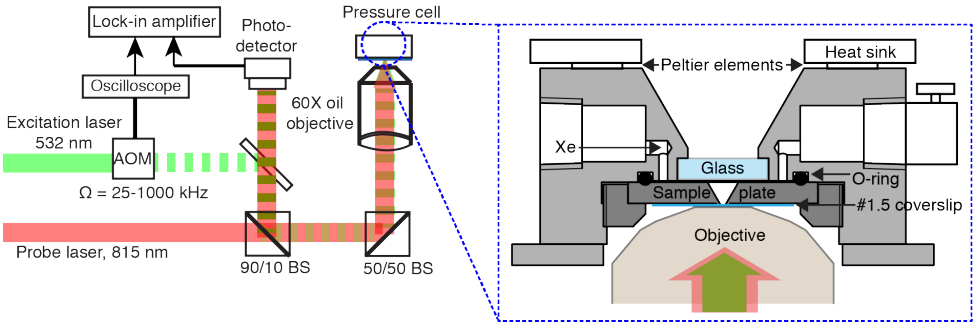

Figure 5.4: Schematic of Optical Setup and Pressure Cell

The optical setup for our experiments is shown in Figure 5.4. The heating beam (532 nm) and the probe beam (815 nm) are focused and overlapped onto the Au NP to achieve the photothermal signal. The diode pumped solid state laser (Coherent Verdi V10) serves as both the heating beam and the pump for a Ti-Sapphire laser (Mira, Coherent) that generates the probe beam. The heating beam is time-modulated via an optical-acoustic modulator at frequencies ranging from 25 kHz to 1 MHz. The beams are expanded five times by a set of lenses (50 mm and 250 mm) to fill the entrance pupil of a 60x 1.3 NA Olympus objective in an inverted microscope configuration. Reflected light is fed into a photodetector (Femto DHPCA-100-F, Germany), with a 532 nm long pass filter placed in front of it to filter out the time modulated 532 nm signals. The time-modulated photothermal signals are extracted from the 815 nm reflected light by a lock-in amplifier.

For control experiments in glycerol at STP, dilute Au nanoparticles were spin-coated on a 0.17 mm thick coverglass, and the sample is mounted onto the stage. The primary novelty of our work is the pressure cell (Figure 5.4), which was designed and machined based on a previous report [83]. Single Au NPs were spin-coated on a 0.17 mm thick coverglass,

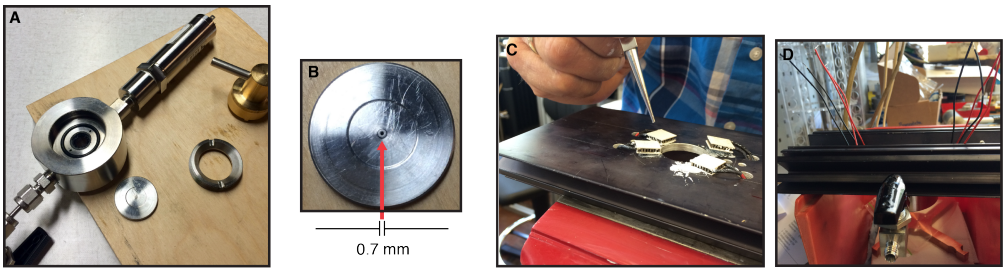

Figure 5.5: Pressure Cell Components

which was then glued via Atomic Adhesive AA- BOND F113 epoxy to a stainless steel plate, giving an optical aperture that is 0.7 mm in diameter (Figure 5.5b). The plate was pushed up against an O-ring inside the pressure chamber to seal the cell. This design allowed us to use a high numerical aperture objective while also operating up to 6.4 MPa of pressure without coverglass rupture. Peltier elements and a heat sink were added to the top of the cell for maintaining temperature control (Figure 5.5 cd). This pressure cell was connected to one side of a 500 ml volume piston, and the pressure of the Xe was regulated by controlling the pressure of nitrogen gas connected to the other side of the piston.

For a routine near-critical Xe measurement, the valve to the 500 ml of the Constant Pressure Cylinder (CPC) from Welker was first closed. The pressure cell containing the sample was connected to the rest of the pressure line (Figure 5.6) at atmospheric conditions. Air is flushed out by introducing low pressure (0.5 MPa) Xe for around ten seconds. Then, the valve connecting to the Welker cylinder was opened and filled with 0.5 MPa Xe from the Xe cylinder. The red portion of the diagram in Figure 5.6 was filled up to a set low pressure. Then, the valve connecting the line to the Xe cylinder is closed, and the pressure of the system is increased by introducing N_2 from the N_2 cylinder to the black portion of the diagram, and using the regulator on the N_2 cylinder, until the desired pressure is reached, as indicated by the pressure meter. This compresses the Xe portion of the CPC that is connected to the pressure cell. After the experiment is completed, N_2 is released via the valve on the CPC, thereby lowering the pressure and expanding the volume of the CPC. In doing this, a large portion of Xe can be stored in the CPC as low pressure Xe and reused for future experiments. The pressure meter is a customized pressure transducer (Omega) that measures pressure range from 0-10 MPa, with an accuracy of 0.025 MPa. Xe 5.0 was purchased from Linde.

5.3.3 Experimental Results

We measured the signal-to-noise ratio (SNR) of 20 nm Au NPs over a range of temperatures and pressures extending from below to above the critical point of Xe, at a heating power of 3.5 μW and probe power of 0.6 mW [84]. The heating laser at 532 nm excites the

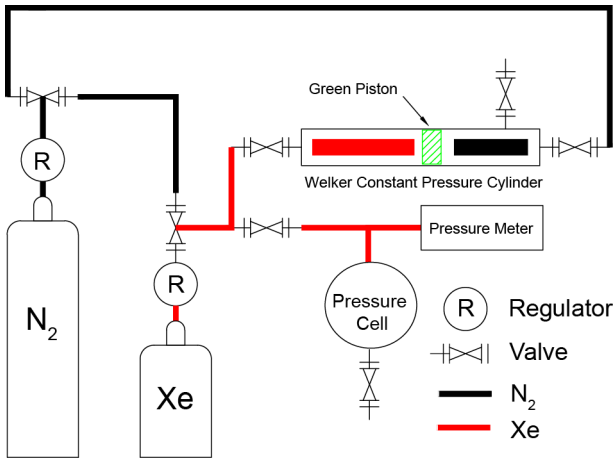

Figure 5.6: Pressure System

surface plasmon resonance of Au NPs, whose absorbed energy then dissipates into the environment as heat. The data presented in Figure 5.7 were obtained on three particles and then normalized appropriately to represent the mean of a distribution of 90 Au NPs whose signals we measured at one T, P condition. We then performed an interpolation of the data set to create a continuous two-dimensional map (Figure 5.7a) of the SNR. Figure 5.7b shows the interpolated map and the measured data set plotted together in the same three-dimensional (3D)- rendered version of Figure 5.7a. In the map, the highest signals traverse a diagonal path, increasing toward the bottom left corner of the map.

The area of the highest thermodynamic sensitivity, and therefore critical divergence, has many unique experimental features. It should have the largest signal, the largest slope, and the largest signal dependence on modulation frequency in the frequency range of 25 kHz to 1 MHz. The first two behaviors are well-depicted by the predictions in Figure 5.3b, caused by the divergence of α_p. The high modulation frequency dependence stems from the divergence of the characteristic thermal time constant τ coupled with the increase in the correlation lengths associated with critical phenomena.

Maximum SNR as a function of temperature is plotted in Figure 5.7c, showing that the highest values were achieved in the range of 13.5–15.5 °C and 5.85–6.01 MPa. Although similar SNR values were achieved at three different conditions (Figure 5.7c), the signal at 13.5 °C exhibits a larger slope than the signal at 15.5 °C. Specifically, an average SNR of 630 at 13.5 °C and 5.85 MPa drops by a factor of 2 over a pressure change of only 0.02 MPa. As a comparison, at 15.5 °C and 6.01 MPa, we measure a similar SNR, but its slope is much smaller, as the signal decreases by a factor of 2 over 0.06 MPa. Because the accuracy of our pressure transducer is 0.025 MPa and we are not using a sophisticated system to maintain precise pressure and temperature conditions down to kilopascal and millikelvin[75], the signals at these highly sensitive regions will be large but noisy. The error bars in Figure 5.7c represent the noise associated with the sensitivity and slope, which noticeably becomes largest at 13.5 °C.

A comparison of signal dependence on modulation frequency for Au in a highly diverging Xe (magenta box in Figure 5.7a) environment, a more weakly diverging Xe (black) environment, and glycerol is plotted in Figure 5.7d. The sharpest drop-off seen for highly diverging

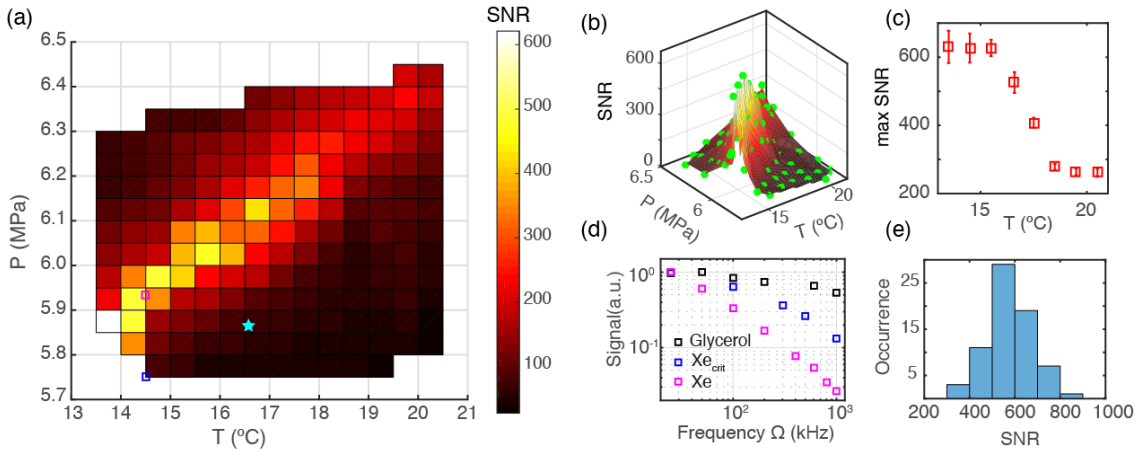

Figure 5.7: Experimental data on the enhancement

Xe is indicative of the increase in the characteristic thermal time constant τ, or likewise, the decrease in the thermal diffusion length r_{th}. Specifically, inputting reported values of C_p and κ for glycerol and critical Xe, we find that from 25 kHz to 1 MHz, r_{th} spans from 780 to 120 nm for critical Xe while it spans from 3 μm to 470 nm for glycerol (compared to ω ≈ 250 nm). We therefore attribute the complex frequency dependence of the photothermal signal in near-critical Xe to the large ranges of spatial and temporal fluctuations close to the critical point.

	Au(d)	P_{heat}	P_{probe}	$\Delta T(K)$	P_{diss}	SNR	$\frac{SNR}{(P_{heat}\sqrt{P_{probe}})}$
glycerol	20nm	210μW	9.4mW	14	492nW	312 ±50	0.48
Xe	20nm	3.5μW	0.6mW	2.2	8nW	620 ±140	230
glycerol	5nm	210μW	20mW	0.84	7.5nW	11.4 ±2.6	0.012
Xe	5nm	1.8μW	1mW	0.057	64pW	9.4 ±2.7	5.2

Table 5.2: Experimental Comparison of SNR of An NPs in Glycerol and Xe

There exists some discrepancy between the predicted and experimental region at which the maximum enhancement occurs. Figure 5.7a shows that the highest sensitivity occurs at temperatures lower than T_c and a pressure higher than P_c (the critical point is represented by the cyan star in Figure 5.7a). We believe that both discrepancies may arise in part from the purity of the Xe gas and in part from local heating by pump and probe beams, which removes fluid layers close to the particle from critical conditions. The change in temperature at the surface of the 20 nm Au NP is around 2.2 K (Table 5.2). Given the high sensitivity of the signal to changes in temperature and pressure as discussed in the previous paragraphs, the local temperature at the surface of the particle is likely higher than the temperature readout in our data. Therefore, one would need to go to lower temperature than T_c to achieve a temperature that is near T_c in the vicinity of the thermo-optical enhancement. Impure Xe also leads to its effective critical point shifting to higher pressure and lower temperature, as well as weaker divergence. One possible source of impurity in the Xe gas may be the effectiveness of the piston separating N_2 gas from Xe. Indeed, we find that the more the Xe is reused, the more the diagonal path in Figure 3a shifts toward the direction of

higher pressure and lower temperature on the map. Furthermore, the modulation frequency depend- ence of the highest signal in the more impure Xe is weaker than that in a fresh batch of Xe, indicative of the weaker divergence.

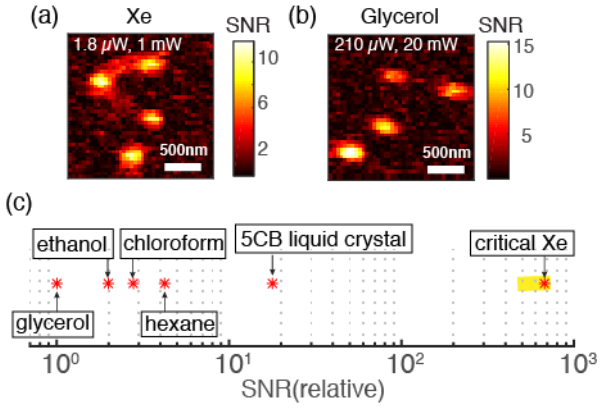

Figure 5.8: Comparison of SNR of Au nanoparticles in near-critical Xe and glycerol

We measured and compared the SNR of 5 and 20 nm Au in glycerol and Xe, shown in Table 5.2. The discrepancy in SNR for 20 and 5 nm particles for each solvent matches the difference in their absorption cross-section within error. Because experiments in glycerol and Xe differ so much in the heating and probe powers used, we calculated the enhancement factor by taking the measurements at the conditions as reported in Table 5.2 and then normalizing by the linear and square root dependence on P_{heat} and P_{probe}, respectively, of the SNR in accordance with eq 5.5. This power-normalized SNR is further normalized to the power-normalized SNR for 20 nm Au NP in glycerol. These values are reported in the last column of Table 5.2 to give a clearer comparison between the sensitivity of the measurement in glycerol and Xe. Using this method, we measure an enhancement factor of 440 ± 130 for experiments in critical Xe over that in glycerol. The enhancement is the same within error for both 5 and 20 nm Au and is similar to the enhancements measured for CO_2 and Xe in photothermal deflection spectroscopy [74, 75].

Notably, 5 nm Au NPs can be detected with SNR of 9.4 at only 1.8 μW of heating power, which is the lowest of any reported in the literature. The operating conditions for similar SNR of 5 nm Au in Xe uses 117 times less heating power and 20 times less probe power than our measurements with glycerol. Photothermal images of 5 nm Au NPs obtained with these different powers in Xe and glycerol are presented side-by- side in panels a and b of Figure 5.8, respectively. Measurement in critical Xe is much more sensitive than in glycerol. It can detect down to 64 pW in absorbed power. This corresponds to 57 mK of change in temperature at the surface of the 5 nm NPs [amplitude $\Delta T = \sigma_{abs} I_{heat}/(4\pi\kappa r)$]. Figure 5.8c shows an overall comparison of the normalized SNR obtained using this method with that using glycerol, common solvents[68], and 5CB liquid crystal as the medium[71, 72]. The yellow region indicates the SNR measured without extensive optimization of pressure and temperature. For example, at the temperature of our optics room, 20.5 °C, we can still obtain signal enhancement of up to 260 (Figure 5.7c). Again, we stress that all experiments were performed above the critical point, or very close to it, so that no bubble could form around the metal NPs. Although bubbles can lead to large photothermal signals[85, 86],

the nucleation process is difficult to control and gives rise to noisy and irreproducible signals that we wished to avoid here. Moreover, bubble formation usually requires significant heating powers, in contrast with our aim in the present work.

5.4 Simultaneous Photothermal and Fluorescence Microscopy of Single QD

Photothermal microscopy poses as a complementary method to shed more information about the photophysics of a given system. We initially had difficulties with the much lower sensitivity of the technique over fluorescence microscopy, as detailed in the last section. In our experiments, because we wish to detect positive or negative correlation between the photothermal and fluorescence channels (Figure 5.2), it would be obsolete if one signal's sensitivity limit is orders of magnitude less than the other. After we improved our photothermal signal by over 400 fold in the previous section using near critical Xe, we sought to 1) examine QD's photothermal and fluorescence intensities simultaneously, 2) analyze the correlation between the two channels, and 3) compare this across particles.

To understand how photothermal microscopy can be applied to semiconductor nanocrystals, as opposed to metal nanoparticles and molecules, we will first examine their electronic structure and optical transitions.

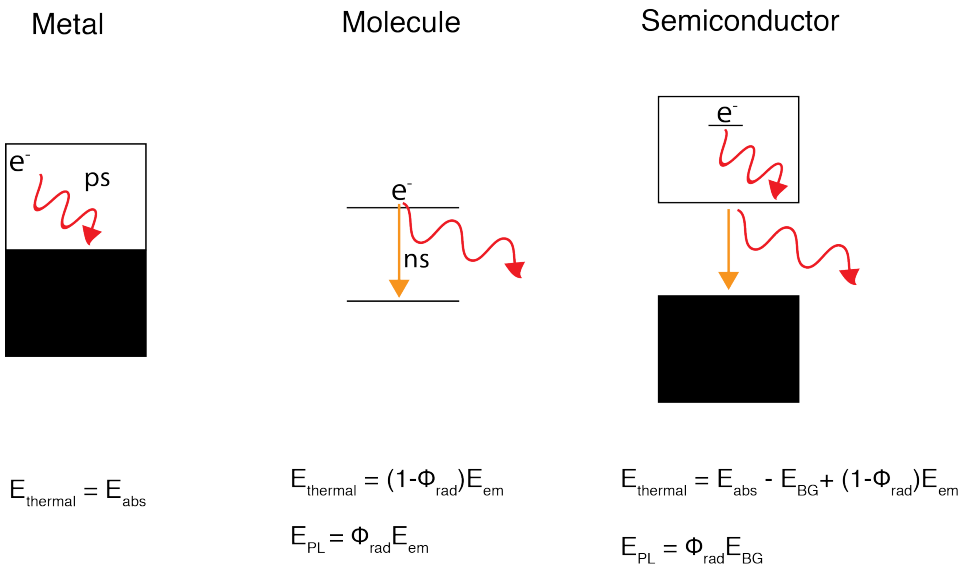

Figure 5.9: Electronic structure of the three types of absorbers

- Metal nanoparticles have been extensively studied via photothermal microscopy because they establish steady-state conditions very rapidly [87, 88]. Thermal relaxation in metals occurs faster than picosecond timescales and nearly all the absorbed light is converted into heat (PLQY of Au nanoparticles are less than tens of a percent [88]). They can withstand the use of high excitation power. For these reasons, metals are the ideal materials for photothermal microscopy. As shown in Figure 5.9, the energy thermalized equals the energy absorbed. Metals also have high absorption coefficients

at the frequency of the surface plasmon resonance relative to molecules and semiconductors (see Table 5.3).

	5 nm Au	molecule	5 nm CdSe QD
Absorption coefficient (nm^2)	3	0.05	0.15
Electron relaxation lifetime	ps	1-10 ns	>10 ns

Table 5.3: Properties of the three types of absorbers

- Molecular absorbers have much slower excited-state decay rates than metals. Their lifetimes are around a few nanoseconds, which greatly limits the excitation power that can be used in the study. The slow relaxation prevents the absorption of another photon and therefore limits the amount of energy converted to heat for a given measurement time, thus lowering the signal. Furthermore, if the molecular dye is in the presence of other dyes, the molecule undergoes singlet-singlet or singlet-triplet annihilation at high power intensity [68]. Many molecular dyes have close to unity PLQYs, but in the case they do not, their emitted heat will be dominated by this nonradiative vibrational relaxation that competes with the radiative emission. Photoexcited electrons with a small probability transfer to triplet states which has microsecond lifetimes. This lifetime slows down the relaxation to steady-state even further. For the most part, in molecules, the thermal energy released is dominated by the nonradiative emission quantum yield.

- Semiconductors are different than molecular dyes and metals in that there could be a large contribution to the thermal energy released from phonon-coupled relaxation to the bandedge. Because semiconductors exhibit a density of states at energy levels extending into the UV and beyond, these materials can be excited at much higher energies than their band gaps. Depending on the excitation energy, the thermal energy released may be a large part of the photothermal signal. The lifetime of semiconductor excited states are also in the range of tens of nanoseconds, which is much slower than for metals. Depending on the PLQY, there will be additional thermal emission via nonradiative relaxation at the bandedge. Therefore, the total thermal emission is a sum of the intraband relaxation and the interband relaxation (Figure 5.9).

Experiments in the next few subsections will discuss examining QDs via photothermal microscopy. QDs used throughout this section will be the same CdSe-core CdS-shell materials that exhibit high native PLQYs. These particles have high photostability on a single particle level, and can persist in air at low flux (average number of exciton <N> less than 0.1) for tens of minutes. The sizes range from 3 ML to 9 ML shell thicknesses, which affect the extent of single particle blinking. Further treatment to the particle such as silica coating and ferrocene functionalization will be discussed as they become relevant throughout the next few sections.

5.4.1 Stability of Native QDs in Near Critical Xe

We first examined these QDs under similar conditions as a previous study [89], under high flux (2 mW) in which tens of excitons are generated on average. Despite this power, it was the first study to implement photothermal microscopy to detecting single QDs. We then applied our critical Xe techniques [84]on these QDs at 20 μW. QDs were unstable in both glycerol and critical Xe when excited at the power conditions that produced photothermal signals.

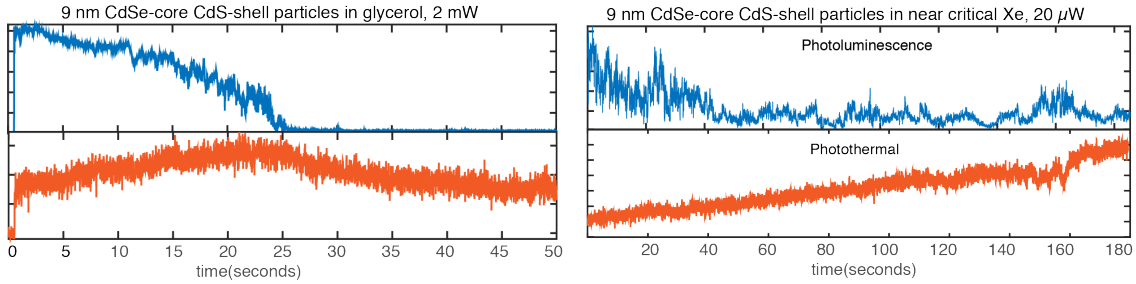

Figure 5.10: PL and photothermal signals of QDs in near critical Xe are unstable.

Native CdSe-core CdS-shell QDs, with oleic acid and phosphonic acid ligands, are not stable due to higher fluence (2 mW) in glycerol, at average exciton, <N>, greater than ten (Figure 5.10). Under these conditions, QDs not only photobleach rapidly but undergo reaction with the medium to growth of the photothermal signal in both the two cases in Figure 5.10. The bleach in PL is expected for these samples at this flux [89]. However, we notice that in glycerol, the photothermal signal grows indefinitely, which is uncharacteristic of any absorber unless a chemical reaction is taking place. Experiments in organic solvents like heptadecane shows stable photothermal signals, which hints that the stability is related to photochemical reactions with alcohol groups of glycerol.

Noticeably, we also discovered that near critical Xe is a highly unstable medium for studies at even low flux, <N> = 1, shown in Figure 5.10. The photoluminescence rapidly diminishes in the first tens of seconds and the indefinite growth of the photothermal signal is exacerbated in near critical Xe. In non-critical Xe, this behavior does not occur and the PL is stable for hours. We attribute the degredation of the QDs to the excellent solvent properties of Xe in these critical conditions, which dissolves the QD surface ligands Cd-ODPA and Cd-OA, leaving an unpassivated QD with a high number of trap states which participate in photo-oxidation of the QD material. Although Xe has no permanent dipole, polarizability scales as the volume which due to Xe's large size contributes to its polarizability. Under supercritical conditions, surface tension does not exist to slow down collisions and therefore enhances the kinetics of the the ligand solvation [90]. It should be noted that despite this excellent solvent ability, there is no oxygen in our Xe medium (99.999% purity) and mechanisms like photo-oxidation should not be able to occur. The loss of surface passivating ligands can create traps that compete with fluorescence, but the growth of the photothermal signal is unexpected and strange.

We therefore sought to apply a thin silica coating on our QDs that will act as a physical barrier from the Xe solvent, while being thin enough to not be a thermal barrier to the

released heat. The thermal diffusion length is typically hundreds of nm length scales, so silica coatings less than 10 nm in thickness should not hinder the photothermal signal response.

5.4.2 Synthesis of Silica-Coated QDs (SC-QD)

IGEPAL CA-630 (a nonionic non-denaturing detergent, 0.6 g), hexane (10 ml), water (60 μl), QDs (d = 8.9 $\pm$0.62 nm, 0.5 nmoles, NH_4OH (30 μl), and a stirbar were added to a 20 ml glass vial. The vial was kept under Ar stirring for 10 minutes. Then, 100 μl of tetraethyl orthosilicate was added and the mixture was left stirring for 20 hours. For workup, a few ml of ethanol were added and the solution was centrifuged in 2 ml volumes at 11000 rpm. The supernatant was decanted and the particles were suspended in ethanol after sonication. The centrifugation step was repeated once more to clean the particles. TEM images, Figure 5.11, show that some particles are clustered while examples of better dispersions also exist. The average thickness of the silica shell, which shows excellent contrast under the TEM was measured to be 6.4 $\pm$ 1.2 nm.

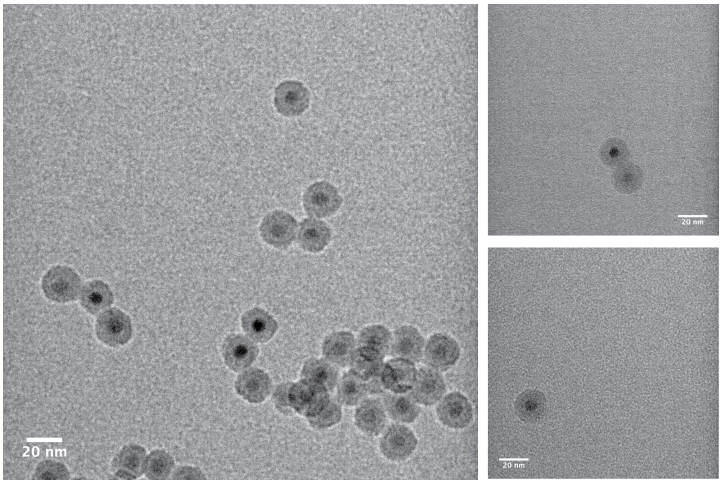

Figure 5.11: TEM images of silica coated QDs

5.4.3 Sample Prep for Optical Microscopy

To make single silica-coated QD dispersions for optical microscopy, these silca-coated QDs (SC-QDs) were diluted to tens of picomolar concentration and spincoated on a cleaned 0.17 mm coverslip (cleaning steps were the same as discussed in the last section for Au). For best dispersions, the proper concentration of quantum dots were sonicated in 40 °C for 10 minutes and then immediately spincoated for one minute at 4000 rpm. If left without sonication for a few minutes, the silica-coated particles aggregate as evidenced by electron and optical microscopy.

For uncoated QD with native ligands, the same dilution was made in hexane, and spin-coated for one minute at 4000 rpm right away.

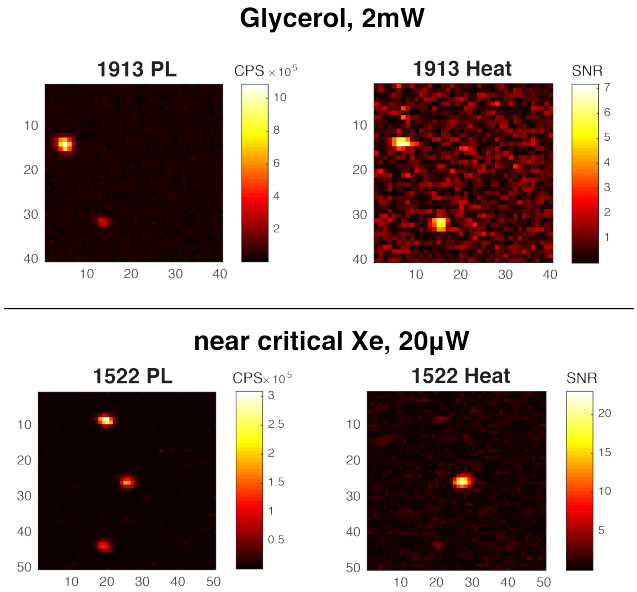

Figure 5.12: QD PL and photothermal signals for the two different mediums

5.4.4 Bleaching of SC-QD's PL and Absorption

SC-QDs exhibit excellent stability under both the conditions that caused degradation for the uncoated particles. In glycerol at high flux and in critical Xe, the SC-QDs' photothermal signals did not grow. Figure 5.12 shows the PL and photothermal maps of quantum dots in glycerol and in near critical Xe at 2 mW and 20 μW, respectively. This low power allows quantum dots to be measured at conditions that are closer to their steady-state optical conditions. Particles show similar photothermal SNR, indicating the 100x improvement in sensitivity that near critical Xe provides to the imaging. This accounts for the first non-fluroescence detection of single QDs at low flux, where the PL and heat emissions are both present. The near critical data in Figure 5.12 is especially interesting. From the PL, we see that all three particles have similar intensities. However, the photothermal map shows that the middle particle has the highest heat emission, indicating that the PLQY of that particle is extremely low.

We examined the photobleaching effects of SC-QDs through their thermal relaxation and fluorescence pathways in glycerol at 2 mW (Figure 5.13). The PL of an absorber is much easier to influence than its absorption. Only one channel, caused by a defect on a lattice or a structural change at a local site on a large molecule like a polymer or a quantum dot, needs to exist to act as a sink for the photoexcited charges of the absorber. Therefore, we postulate that as particles degrade, the photoluminescence should diminish first, with the absorption of the molecule or QD persisting longer. Structural change to a larger portion of the material needs to occur to influence the probability of the absorption transition.

In Figure 5.13, we see a variety of correlations between the two channels, which informs us of the diversity of photodegradation pathways for these QDs. Particle A, B, C, and F exhibit first the bleaching of the PL signal, followed by a marked decrease in the photothermal signal one to ten seconds after the PL bleach. The photothermal bleach is an indication of the structural decomposition that affects the electronic transition probability of the QD at 532

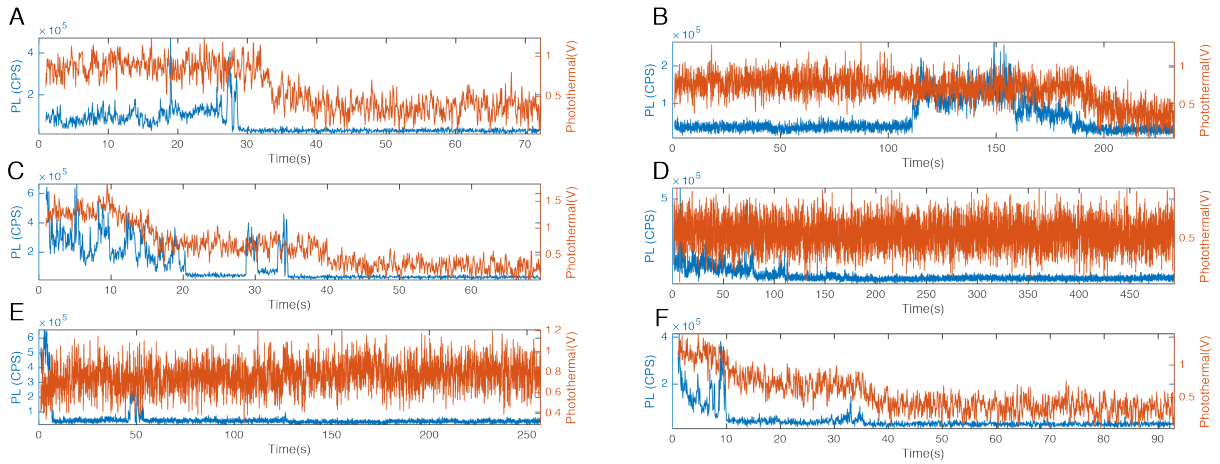

Figure 5.13: Silica-stability in glycerol at 2 mW

nm. In Particle C and F, there are two regions in the time trajectory where the absorption drops, both following a transient increase in the fluorescent signature. This shows that the degradation may not proceed continuously. Particle D and E show photothermal signals that have no detectable signal change.

The decrease in PL should not translate to a higher photothermal signal in these measurements because the sensitivity of the photothermal channel is about 1000 times less than that of the PL since we are operating in glycerol. In other words, the energy associated with the photons being emitted would be a miniscule value compared to the energy being emitted as heat. This is because at this high flux, the quantum yield is less than 1% due to multiexciton nonradiative decay. Therefore, the photothermal signal can be thought of as the absorption signal of the material. Nevertheless, this set of data is informative of the photoactivated decay of the fluorescence and absorption of QDs. The bleach of both the PL and photothermal over a few seconds in most of these particles is likely associated with an important structural change. In these CdSe-core CdS-shell particles, PL occurs at the CdSe core. Furthermore, 532 nm corresponds mostly to absorption of CdSe rather than CdS. Therefore, it may be that the decomposition process which occurs from the exterior to the interior proceeds continuously over time, but is not detected by the photothermal channel which corresponds only to the core. When the decomposition reaches the core, then the material that is responsible for the absorption at 532 nm finally degrades and causes the absorption coefficient to diminish.

5.4.5 SC-QD photothermal and fluorescence at low flux

We were able to measure the photothermal signals of SC-QDs at 20 μW, which corresponds to an average exciton of 1. This value is still much higher than typical fluorescence microscopy, which occurs at biexciton average of less than 0.1. The photoluminescence is centered at 627 nm. Table 5.4 shows the theoretical energies emitted as heat versus as photons for this given system. For reference, A is the absorption energy, E_{BG} is the energy of the bandedge emission. PL_{tot} is the energy associated with PL emission, which depends on the PLQY. PT_{inter} is the energy of the nonradiative emission at the bandedge which com-

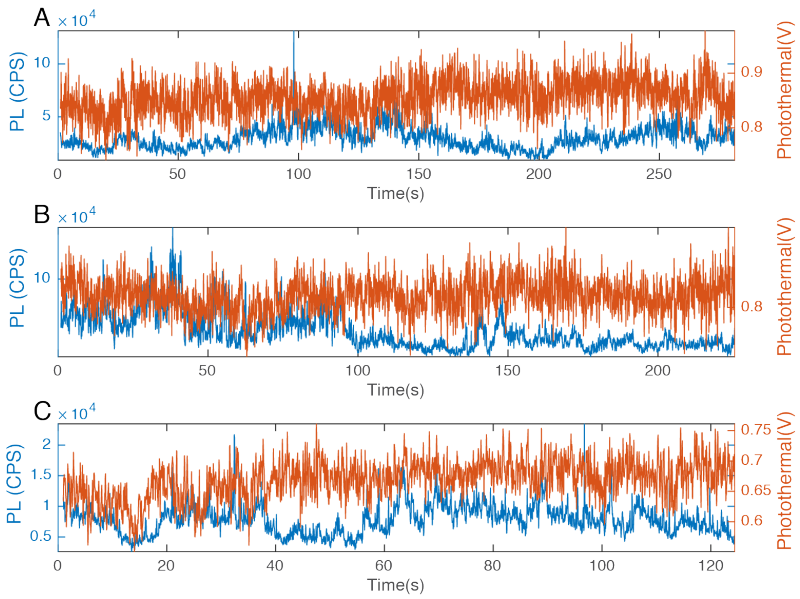

Figure 5.14: PL and photothermal signals of silica-coated QDs, taken at 20μW

plements PL_{tot}. PT_{intra} is the energy dissipated as heat through relaxation to the minimum of the conduction band. PT_{tot} is the total photothermal energy which is just the sum of the two PT energies in the last two columns. In the SC-QD with 70% PLQY, we see that 60% of the photothermal signal comes from nonradiative bandedge emission with the rest coming from the electron relaxation to the conduction band.

	PLQY	A(nm/eV)	E_{BG}(nm/eV)	PL_{tot}(eV)	PT_{inter}(eV)	PT_{intra}(eV)	PT_{tot}(eV)
9nm	70%	532/2.34	627/1.98	1.39	0.36	0.59	0.95
6nmFc	3%	532/2.34	601/2.07	0.06	0.09	2.01	2.1

Table 5.4: Energies of radiative and nonradiative channels

Figure 5.14 shows photothermal and PL time traces of silica-coated QDs at 20 μW of power in near-critical Xe. We note that while native single particle QDs exhibit discrete on and off trajectories, these silica-coated QDs do not. This makes understanding the correlation between the two channels difficult to resolve as there are not any large fluctuations in the PL intensities. The correlation is chemically less probable due to lack of blinking. Furthermore, the sensitivities of the two channels are still not equal. A factor of ten difference in the sensitivities means that all PL converted to heat would cause about a 10% change in the current photothermal signal intensities. The noise of our measurement technique is high, which makes small changes in the signal difficult to detect.

5.4.6 QY differences for SC-QDs with ferrocene quencher

We present preliminary data on the the photothermal-PL maps of two sets of QDs with different PLQYs, depicted in Figure 5.15. One sample is the 70% PLQY silica-coated 9 nm SC-QD and the other is 3% PLQY 6 nm SC-QD functionalized with FcC3SH, as investigated

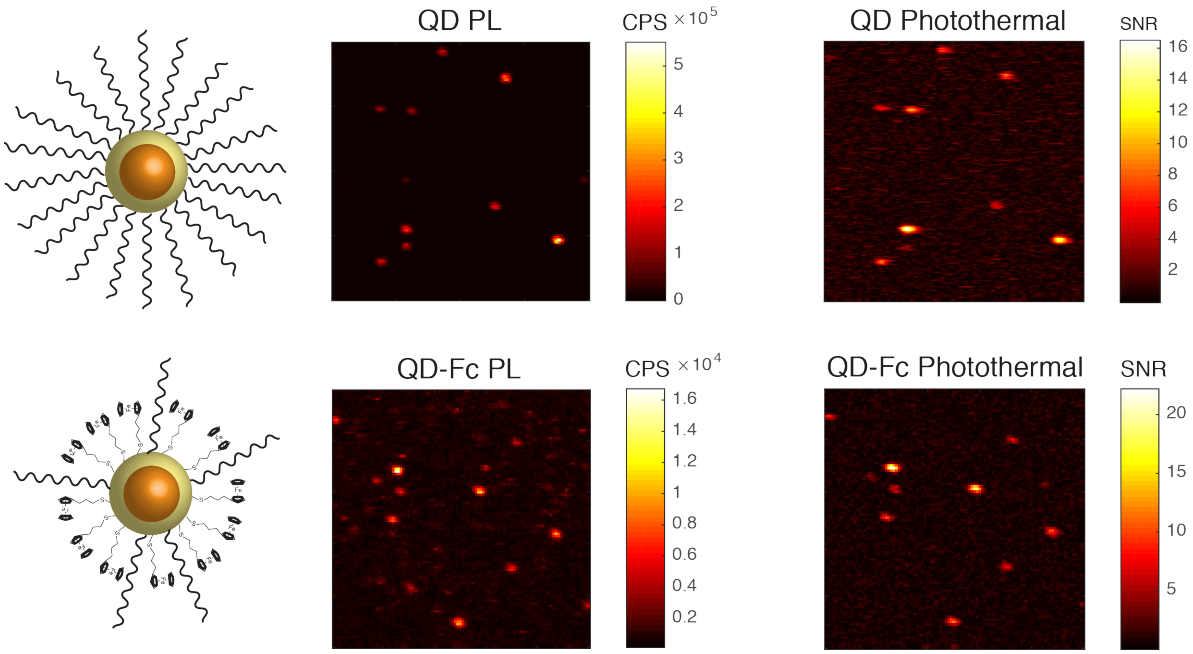

Figure 5.15: 10 μm by 10 μm maps of the PLQY and photothermal of QDs with and without full coverage of ferrocene acceptors.

in Chapter 2 and Chapter 3. We used the same charge transfer system to prepare quantum dots with controllably different PLQY by hole transfer to ferrocene without changing the actual material properties of the QDs. The energies emitted as radiative emission, thermal relaxation to bandedge, and nonradiative bandedge emission for these two systems are shown in Table 5.4. Note that in addition, the absorption coefficients at 532 nm are different for the two samples. Taken into consideration all these parameters, we expect the photothermal signals to be comparable for these two samples and for the PL signals to be very different due to the effect of hole quenching by ferrocene in the second system. Based on the difference in ensemble quantum yields, we should expect to see PL intensities that are about 20x less in QDs covered with Fc. Figure 5.15 shows PL and photothermal maps of the two systems, with noticeable differences in PL intensity but similar intensities for photothermal. On average, the PL intensities of SC-QDs packed with Fc are 25x less than that of SC-QDs without Fc, which is similar to the ensemble data.

Future work needs to quantitatively determine the PLQY of these individual particles and examine the statistics of that data, which will elucidate the heterogeneity of these samples.

Chapter 6

Concluding Remarks

We designed and synthesized a quantum dot charge transfer model system for understanding its limitations in QD-sensitized solar cells and QD photocatalytic systems. This model system utilizes CdSe-core CdS-shell QD as the photoexcited hole donor and with ferrocene as acceptor, with a well-defined spacing and material between them. We conducted an empirical investigation of the dependence of charge transfer rate on electronic coupling, thermodynamic driving force, and reorganization energy in context of the Marcus Theory for Charge Transfer. Our system allowed us to study these parameters in a well-defined manner, and the rate constant per acceptor can be extracted and used to compare from system to system. Electronic coupling studies allowed us to understand tunneling through CdS and organic alkyl chains. Driving force results did not agree with a two-state charge transfer model, and led to postulation of new mechanistic model with a multitude of final states to explain the lack of an inverted region. Knowing how to moeculate hole transfer rate constants gives us synthetic tunability over the desired rate constant. If we had complementary data on electron transfer on the same system, we would be able design photocatalytic systems for which the hole and electron transfer rates to their respective acceptors are well-matched.

We also studied charge dynamics in quantum dots on a single particle level. To this end, we developed photothermal microscopy as a method to probe the nonradiative decay of QDs simultaneously with its fluorescence. By having a handle on both these channels, we can explore their correlation over time which is insightful for understanding mechanisms of photophysics in not only quantum dots, but also molecules. Using near critical Xe, we enhanced the sensitivity of photothermal microscopy by 400x. Using this method, we conducted the first low power simultaneous measurements of the photothermal and fluorescence of single QDs. From this, photoluminescence quantum yields of single particles can be calculated. Examining many particles, we would be able to build a body of statistics on the heterogeneity of a given QD sample.

Bibliography

[1] Shirasaki, Y.; Supran, G. J.; Bawendi, M. G.; Bulović, V. *Nature Photonics* **2012**, *7*, 13–23.

[2] Medintz, I. L.; Uyeda, H. T.; Goldman, E. R.; Mattoussi, H. *Nature Materials* **2005**, *4*, 435–446.

[3] Kramer, I. J.; Sargent, E. H. *Chemical Reviews* **2014**, *114*, 863–882.

[4] Chuang, C.-H. M.; Brown, P. R.; Bulović, V.; Bawendi, M. G. *Nature Materials* **2014**, *13*, 796–801.

[5] Kamat, P. V.; Christians, J. A.; Radich, J. G. *Langmuir* **2014**, *30*, 5716–5725.

[6] Marcus Rudolph. A., S. N. *Biochim. Biophys. Acta, Rev. Bioenerg.* **1985**, *811*, 265.

[7] Miller, J. R.; Calcaterra, L. T.; Closs, G. L. *Journal of the American Chemical Society* **1984**, *106*, 3047–3049.

[8] Knowles, K. E.; Peterson, M. D.; McPhail, M. R.; Weiss, E. A. *Journal of Physical Chemistry C* **2013**, *117*, 10229–10243.

[9] Wu, K.; Chen, Z.; Lv, H.; Zhu, H.; Hill, C. L.; Lian, T. *Journal of the American Chemical Society* **2014**, *136*, 7708–7716.

[10] Klimov, V. I.; McBranch, D. W.; Leatherdale, C. A.; Bawendi, M. G. *Physical Review B* **1999**, *60*, 13740–13749.

[11] Fisher, B. R.; Eisler, H.-J.; Stott, N. E.; Bawendi, M. G. *The Journal of Physical Chemistry B* **2004**, *108*, 143–148.

[12] Chaban, V. V.; Prezhdo, V. V.; Prezhdo, O. V. *The Journal of Physical Chemistry Letters* **2013**, *4*, 1–6.

[13] Gray, H. B.; Winkler, J. R. *Proceedings of the National Academy of Sciences* **2005**, *102*, 3534–3539.

[14] Li, X.; Nichols, V. M.; Zhou, D.; Lim, C.; Pau, G. S. H.; Bardeen, C. J.; Tang, M. L. *Nano Letters* **2014**, *14*, 3382–3387.

[15] Morris-Cohen, A. J.; Frederick, M. T.; Cass, L. C.; Weiss, E. A. *Journal of the American Chemical Society* **2011**, *133*, 10146–10154.

[16] Huang, J.; Huang, Z.; Jin, S.; Lian, T. *Journal of Physical Chemistry C* **2008**, *112*, 19734–19738.

[17] Chen, O.; Zhao, J.; Chauhan, V. P.; Cui, J.; Wong, C.; Harris, D. K.; Wei, H.; Han, H.-S.; Fukumura, D.; Jain, R. K.; Bawendi, M. G. *Nature Materials* **2013**, *12*, 1–7.

[18] Yu, W. W.; Qu, L.; Guo, W.; Peng, X. *Chemistry of Materials* **2003**, *15*, 2854–2860.

[19] Wider, G.; Dreier, L. *Journal of the American Chemical Society* **2006**, *128*, 2571–2576.

[20] She, C.; Demortière, A.; Shevchenko, E. V.; Pelton, M. *The Journal of Physical Chemistry Letters* **2011**, *2*, 1469–1475.

[21] Bronstein, N. D.; Yao, Y.; Xu, L.; O'Brien, E.; Powers, A. S.; Ferry, V. E.; Alivisatos, A. P.; Nuzzo, R. G. *ACS Photonics* **2015**, 150821134054007.

[22] Müller-Meskamp, L.; Karthäuser, S.; Waser, R.; Homberger, M.; Wang, Y.; Englert, U.; Simon, U. *Surface Science* **2009**, *603*, 716–722.

[23] Tindale, J. J.; Hartlen, K. D.; Alizadeh, A.; Workentin, M. S.; Ragogna, P. J. *Chemistry - A European Journal* **2010**, *16*, 9068–9075.

[24] Schapotschnikow, P.; Hommersom, B.; Vlugt, T. J. H. *Journal of Physical Chemistry C* **2009**, *113*, 12690–12698.

[25] Hassinen, A.; Moreels, I.; De Nolf, K.; Smet, P. F.; Martins, J. C.; Hens, Z. *Journal of the American Chemical Society* **2012**, *134*, 20705–20712.

[26] Puzder, A.; Williamson, A. J.; Zaitseva, N.; Galli, G.; Manna, L.; Alivisatos, A. P. *Nano Letters* **2004**, *4*, 2361–2365.

[27] Gomes, R.; Hassinen, A.; Szczygiel, A.; Zhao, Q.; Vantomme, A.; Martins, J. C.; Hens, Z. *The Journal of Physical Chemistry Letters* **2011**, *2*, 145–152.

[28] Ding, T. X.; Olshansky, J. H.; Leone, S. R.; Alivisatos, A. P. *Journal of the American Chemical Society* **2015**, *137*, 2021–2029.

[29] Tarafder, K.; Surendranath, Y.; Olshansky, J. H.; Alivisatos, A. P.; Wang, L.-W. *Journal of the American Chemical Society* **2014**, *136*, 5121–5131.

[30] Dorokhin, D.; Tomczak, N.; Velders, A. H.; Reinhoudt, D. N.; Vancso, G. J. *Journal of Physical Chemistry C* **2009**, *113*, 18676–18680.

[31] Wuister, S. F.; de Mello Donegá, C.; Meijerink, A. *The Journal of Physical Chemistry B* **2004**, *108*, 17393–17397.

[32] Munro, A. M.; Jen-La Plante, I.; Ng, M. S.; Ginger, D. S. *Journal of Physical Chemistry C* **2007**, *111*, 6220–6227.

[33] Ji, X.; Copenhaver, D.; Sichmeller, C.; Peng, X. *Journal of the American Chemical Society* **2008**, *130*, 5726–5735.

[34] Zhu, H.; Song, N.; Lian, T. *Journal of the American Chemical Society* **2010**, *132*, 15038–15045.

[35] Adams, D. M.; Brus, L.; Chidsey, C. E. D.; Creager, S.; Creutz, C.; Kagan, C. R.; Kamat, P. V.; Lieberman, M.; Lindsay, S.; Marcus, R. A.; Metzger, R. M.; Michel-Beyerle, M. E.; Miller, J. R.; Newton, M. D.; Rolison, D. R.; Sankey, O.; Schanze, K. S.; Yardley, J.; Zhu, X. *The Journal of Physical Chemistry B* **2003**, *107*, 6668–6697.

[36] Sykora, M.; Petruska, M. A.; Alstrum-Acevedo, J.; Bezel, I.; Meyer, T. J.; Klimov, V. I. *Journal of the American Chemical Society* **2006**, *128*, 9984–9985.

[37] Inkpen, M. S.; Du, S.; Driver, M.; Albrecht, T.; Long, N. J. *Dalton Transactions* **2013**, *42*, 2813–2816.

[38] Olshansky, J. H.; Ding, T. X.; Lee, Y. V.; Leone, S. R.; Alivisatos, A. P. *Journal of the American Chemical Society* **2015**, *137*, 15567–15575.

[39] Zhu, H.; Yang, Y.; Hyeon-Deuk, K.; Califano, M.; Song, N.; Wang, Y.; Zhang, W.; Prezhdo, O. V.; Lian, T. *Nano Letters* **2014**, *14*, 1263–1269.

[40] Hyeon-Deuk, K.; Kim, J.; Prezhdo, O. V. *The Journal of Physical Chemistry Letters* **2015**, *6*, 244–249.

[41] Canovas, E.; Moll, P.; Jensen, S. A.; Gao, Y.; Houtepen, A. J.; Siebbeles, L. D. A.; Kinge, S.; Bonn, M. *Nano Letters* **2011**, *11*, 5234–5239.

[42] Klimkāns, A.; Larsson, S. *Chemical Physics* **1994**, *189*, 25–31.

[43] Smalley, J. F.; Feldberg, S. W.; Chidsey, C.; Linford, M. R.; Newton, M. D.; Liu, Y. P. *Journal of Physical Chemistry* **1995**, *99*, 13141–13149.

[44] Liu, Y. P.; Newton, M. D. *The Journal of Physical Chemistry* **1994**.

[45] Widmer-Cooper, A.; Geissler, P. L. *Nano Letters* **2013**, *14*, 57–65.

[46] Gray, H. B.; Malmström, B. G.; Williams, R. J. P. *Journal of Biological Inorganic Chemistry* **2000**, *5*, 551–559.

[47] De Roo, J.; Ibáñez, M.; Geiregat, P.; Nedelcu, G.; Walravens, W.; Maes, J.; Martins, J. C.; Van Driessche, I.; Koyalenko, M. V.; Hens, Z. *ACS Nano* **2016**, *10*, 2071–2081.

[48] Anderson, N. C.; Hendricks, M. P.; Choi, J. J.; Owen, J. S. *Journal of the American Chemical Society* **2013**, *135*, 18536–18548.

[49] Yang, Y.; Qin, H.; Peng, X. *Nano Letters* **2016**, *16*, 2127–2132.

[50] Yang, Y.; Qin, H.; Jiang, M.; Lin, L.; Fu, T.; Dai, X.; Zhang, Z.; Niu, Y.; Cao, H.; Jin, Y.; Zhao, F.; Peng, X. *Nano Letters* **2016**, *16*, 2133–2138.

[51] Widmer-Cooper, A.; Geissler, P. L. *ACS Nano* **2016**, *10*, 1877–1887.

[52] Frederick, M. T.; Achtyl, J. L.; Knowles, K. E.; Weiss, E. A.; Geiger, F. M. *Journal of the American Chemical Society* **2011**, *133*, 7476–7481.

[53] Weeraman, C.; Yatawara, A. K.; Bordenyuk, A. N.; Benderskii, A. V. *Journal of the American Chemical Society* **2006**, *128*, 14244–14245.

[54] Guyotsinnest, P.; Hunt, J. H.; Shen, Y. R. *Physical Review Letters* **1987**, *59*, 1597–1600.

[55] Ashby, M. T. *Journal of Chemical Education* **2007**.

[56] Glasser, L. *Journal of Chemical Education* **1979**, *56*, 22–23.

[57] Fritzinger, B.; Capek, R. K.; Lambert, K.; Martins, J. C.; Hens, Z. *Journal of the American Chemical Society* **2010**, *132*, 10195–10201.

[58] Garcia-Rodriguez, R.; Liu, H. *Chemical Communications* **2013**, *49*, 7857.

[59] Nirmal, M.; Dabbousi, B. O.; Bawendi, M. G.; Macklin, J. J.; Trautman, J. K.; Harris, T. D.; BRUS, L. E. *Nature* **1996**, *383*, 802–804.

[60] Borys, N. J.; Walter, M. J.; Huang, J.; Talapin, D. V.; Lupton, J. M. *Science* **2010**, *330*, 1371–1374.

[61] Ebenstein, Y.; Mokari, T.; Banin, U. *Applied Physics Letters* **2002**, *80*, 4033.

[62] Ha, T.; Tinnefeld, P. *Annual Review of Physical Chemistry* **2012**, *63*, 595–617.

[63] Lakowicz, J. *Principles of Fluorescence Spectroscopy*; Springer: New York, 2007.

[64] Gaiduk, A.; Yorulmaz, M.; Ruijgrok, P. V.; Orrit, M. *Science* **2010**, *330*, 353–356.

[65] Celebrano, M.; Kukura, P.; Renn, A.; Sandoghdar, V. *Nature photonics* **2011**, *5*, 95–98.

[66] Kukura, P.; Celebrano, M.; Renn, A.; Sandoghdar, V. *The Journal of Physical Chemistry Letters* **2010**, *1*, 3323–3327.

[67] Chong, S.; Min, W.; Xie, X. S. *The Journal of Physical Chemistry Letters* **2010**, *1*, 3316–3322.

[68] Gaiduk, A.; Yorulmaz, M.; Ishow, E.; Orrit, M. *ChemPhysChem* **2011**, *13*, 946–951.

[69] Berciaud, S.; Lasne, D.; Blab, G. A.; Cognet, L.; Lounis, B. *Physical Review B* **2006**.

[70] Bialkowski, S. *Photothermal Spectroscopy Methods for Chemical Analysis*; Wiley: New York, 1996.

[71] Parra-Vasquez, A. N. G.; Oudjedi, L.; Cognet, L.; Lounis, B. *The Journal of Physical Chemistry Letters* **2012**, *3*, 1400–1403.

[72] Chang, W.-S.; Link, S. *The Journal of Physical Chemistry Letters* **2012**, *3*, 1393–1399.

[73] Heber, A.; Selmke, M.; Cichos, F. *ACS Nano* **2014**, *8*, 1893–1898.

[74] Leach, R. A.; Harris, J. M. *Analytical Chemistry* **1984**, *56*, 1481–1487.

[75] Briggs, M. E.; Gammon, R. W. *International journal of thermophysics* **1995**, *16*, 1439–1453.

[76] Sifner, O.; Klomfar, J. *Journal of Physical and Chemical Reference Data* **1994**, *23*, 63–152.

[77] Hanley, H.; McCarty, R. D. *Journal of Physical and ...* **1974**.

[78] Habgood, H. W.; Schneider, W. G. *Canadian Journal of ...* **1954**.

[79] Garside, D. H.; Molgaard, H. V.; Smith, B. L. *Journal of Physics Part B Atomic and Molecular Physics* **1968**, *1*, 449–&.

[80] Stanley, H. *Introduction to Phase Transitions and Critical Phenomena*; Oxford University Press: New York, 1971.

[81] Smith, I. W.; Giglio, M.; Benedek, G. B. *Physical review letters* **1971**, *27*, 1556–1560.

[82] Gaiduk, A.; Ruijgrok, P. V.; Yorulmaz, M.; Orrit, M. *Chemical Science* **2010**.

[83] Pagliaro, L.; Reitz, F.; Wang, J. *Undersea & hyperbaric medicine : journal of the Undersea and Hyperbaric Medical Society, Inc* **1995**, *22*, 171–181.

[84] Ding, T. X.; Hou, L.; Meer, H. v. d.; Alivisatos, A. P.; Orrit, M. *The Journal of Physical Chemistry Letters* **2016**, *7*, 2524–2529.

[85] Nedosekin, D. A.; Galanzha, E. I.; Dervishi, E.; Biris, A. S.; Zharov, V. P. *Small* **2014**, *10*, 135–142.

[86] Hou, L.; Yorulmaz, M.; Verhart, N. R.; Orrit, M. *New Journal of Physics* **2015**, *17*, 1–9.

[87] Boyer, D.; Tamarat, P.; Maali, A.; Lounis, B.; Orrit, M. *Science* **2002**, *297*, 1160–1163.

[88] Yorulmaz, M.; Khatua, S.; Zijlstra, P.; Gaiduk, A.; Orrit, M. *Nano Letters* **2012**, *12*, 4385–4391.

[89] Berciaud, S.; Cognet, L.; Lounis, B. *Nano Letters* **2005**, *5*, 2160–2163.

[90] Rentzepis, P. M.; Douglass, D. C. *Nature* **1981**, *293*, 165–166.